



**HAL**  
open science

# Inference of the Bottom Properties in Shallow Ice Approximation Models

Jerome Monnier, P.-E Des Boscs

► **To cite this version:**

Jerome Monnier, P.-E Des Boscs. Inference of the Bottom Properties in Shallow Ice Approximation Models. 2016. hal-01356778v1

**HAL Id: hal-01356778**

**<https://hal.science/hal-01356778v1>**

Preprint submitted on 26 Aug 2016 (v1), last revised 25 Feb 2017 (v2)

**HAL** is a multi-disciplinary open access archive for the deposit and dissemination of scientific research documents, whether they are published or not. The documents may come from teaching and research institutions in France or abroad, or from public or private research centers.

L'archive ouverte pluridisciplinaire **HAL**, est destinée au dépôt et à la diffusion de documents scientifiques de niveau recherche, publiés ou non, émanant des établissements d'enseignement et de recherche français ou étrangers, des laboratoires publics ou privés.

# Inference of the Bottom Properties in Shallow Ice Approximation Models

J. Monnier, P.-E. des Bosc

INSA & Mathematics Institute of Toulouse, F-31077 Toulouse cedex 4, France.

jerome.monnier@insa-toulouse.fr

This study proposes a new inverse method to infer the bottom topography and the friction coefficient in the Shallow Ice Approximation models (lubrication type models for generalized Newtonian fluid flows). The method is based on sub-regime definitions corresponding to different slip ratios; then combinations of explicit field expressions with an elliptic linear-quadratic optimal control problem (solved by variational data assimilation) lead to depth estimations; next the friction field can be deduced. The numerical results performed on realistic multi-regime flows demonstrate the robustness of the method even in presence of uncertain surface measurements and independently of the depth measurement locations (on contrary if inverting a regularized first order transport equation). A method by-product is to make possible the determination of the adequate slope scale of in the shallow flow model. The method can be straightforwardly extended to unsteady flows if time-dependent surface observations (elevation and velocity) are available.

**Keywords.** Shallow flow, Shallow Ice Approximation, topography inference, friction, data assimilation, glaciers.

## 1 Introduction

The knowledge of the bottom topography is a basic step to set up a numerical flow model; however this crucial data may be unknown or difficult to acquire especially in geophysics. Inverse methods to infer the topography, and potentially the basal slipperiness, are then the only alternative (for a review on inverse methods in free surface flows see e.g. [39]). The bottom topography knowledge combined with the top surface measurements gives straightforwardly a volume - mass estimation; the next important quantity to estimate is the flux. For ice flows, these estimations are important in the context of global warming and sea level rise.

An extra difficulty of shallow flow inverse modeling is the following: even if the free surface presents very small and smooth variations, the bottom topography may not. Indeed, the shallow fluid flows (even newtonian) act as low-band filters: the bed variations are filtered by the flow. The filtering features depend on the sliding amount at bottom, see [13][12] [26] [24] for detailed analysis applied to generalized newtonian / ice flows.

In the case of no-slip at bottom, the inference of the bottom properties is limited to the topography only. Then the difficulty of the corresponding inverse problem depends on the observation availability. In the case of sliding at bottom (or equivalently finite friction), the inverse problem becomes much more difficult since the unknown becomes the (topography, friction) pair. Then a challenging goal is to separate the signature of these two different bottom properties (topography and friction), usually given surface observations - measurements. Under some flow conditions, these two features can lead to equivalent bottom conditions hence making the inference of the property pair particularly challenging, see e.g. [16][4][7] in the Newtonian case (shallow water flows) and [12] [26] in the power-law / Glen-Nye's law case.

The direct measurements of ice thickness, for example along a track using airborne radio-echo sounding, are time-consuming, expensive and provide very sparse measurements only. Also radio-echo sounding can be inaccurate due to water beneath the glaciers e.g. in southern Greenland. The current bedrock maps for Greenland [2] and Antarctica [6] are available at 1 km resolution from measurement surveys plus Kriging interpolation techniques (with simple relations based on the surface slope). But the uncertainty between the measurements still prevent to set up high resolution dynamic ice flow models; and despite the important measurement campaigns, e.g. NASA Operation Ice Bridge. In other respect, various satellites provide quite accurate and frequent ( $\approx 10$  days revisits) measurements of the ice sheet surfaces: altimeters provide the surface elevation  $H(x, t)$  at  $\approx +/- 10 - 30$  cm for 1 km<sup>2</sup> pixels, while radar interferometers (InSar) provide the surface

velocity  $\mathbf{u}_H$  (more or less accurately depending on its magnitude, see e.g. [37]). For non ice-sheet glaciers, e.g. Arctic, Alaska, Patagonia or High Mountains, in-situ measurements are usually the surface elevation while velocity measurements are less usual.

50 A great challenge is to fill up the gaps between the reliable depth measurements and to determine an effective slipperiness (modeling basal conditions e.g. till or subglacial hydrology networks). This goal can be partially reached by developing inverse methods combining all available information.

Let us introduce some notations, the standard depth-averaged mass equation and the classical Shallow Ice Approximation (SIA) equation (standard lubrication approximation). The surface flow elevation is denoted by  $H$ , the bed elevation is denoted by  $b$  and the ice depth (or thickness) is defined by  $h$ ,  $h = (H - b)$ , see Fig. 1. Then the depth-averaged mass equation reads:

$$\operatorname{div}(h\bar{\mathbf{u}}) = a - \partial_t h \equiv \dot{a}$$

where  $\bar{\mathbf{u}}$  is the depth-averaged velocity and  $a$  is the mass balance source term. The traditional Shallow Ice Approximation (SIA) (lubrication type equation) is obtained by injecting the velocity expression  $\bar{\mathbf{u}}$  (which can be derived explicitly) into the mass equation above, see e.g. [10, 5]. This gives:

$$-\operatorname{div}_{xy}(\alpha h^5 |\nabla H|^2 \nabla H) = \dot{a}$$

where  $\alpha$  is a coefficient depending on the ice properties. This SIA model version is qualified of “traditional” since no slip is considered at bottom i.e.  $\mathbf{u}_b = 0$  (hence no friction coefficient  $C$  appears in the equation). More details on the shallow flow model derivations are presented in the manuscript.

The inference of the bottom properties (usually the topography only) by inverting a ice model has been addressed in numerous studies. First let us mention the pioneer article [36]. The ice depth  $h$  or/and the effective mass balance  $\dot{a}$  are inferred from the depth-averaged mass equation combined with some surface elevation data  $H^{obs}$ , surface velocity data  $\mathbf{u}_H^{obs}$  and depth measurements  $h^{obs}$  available along flight tracks over the Columbia glacier in Alaska. In the mass equation, the mean velocity is empirically related to the surface velocity by a coefficient  $\gamma$ ,  $\gamma = \bar{\mathbf{u}}/\mathbf{u}_H$ . (Remark that given the power-law exponent of the fluid,  $\gamma$  defines the vertical velocity profile; somehow this spatially-distributed coefficient  $\gamma$  provides a velocity model, replacing the missing momentum equation). Next a quadratic cost function measuring the differences between the model output and the surface velocity measurements is defined. Finally the first-order optimality condition (gradient of the cost function vanishes) is numerically solved by the Newton algorithm. Note that this pioneer study has been carried out before the classical use of the optimal control techniques in data assimilation problems, see e.g. [22], and before the acquisition of rich satellite measurements. In [42], the authors employ the explicit depth expression in function of the SIA equation flux:  $h^5 = \frac{1}{\alpha} \frac{\Phi}{|\nabla H|^3}$ , where the flux  $\Phi$  is estimated by inverting the divergence operator (given  $\dot{a}$ ). An other pioneer study is [41] since it does not address the topography inference only but the (topography  $b$ , friction  $C$ ) pair inference. This is done for fast-flowing ice-streams (unsheared flows) hence not modeled by the SIA equation. The inference is based on the linearized model equation and the analysis of the transmission of flow disturbances through the ice thickness and from surface observations (elevation, velocity). More recently [34] [35] have elaborated a combination of efficient computational algorithms based on a Variational Data Assimilation (VDA), solving the same equations than [36]. The resulting algorithm combined with multi-sources and heterogeneous data sets leads to nice bed maps at  $\approx 300$  m resolution in the challenging South Greenland regions where airborne radar sounding are inaccurate, see [32, 33]. However the method has few drawbacks since it relies on a transport equation, hyperbolic first order. Indeed the equation feature limits the inversion capabilities at locations downstream the depth measurements. In other words, data are required at the characteristic inflow locations. Furthermore the hyperbolic feature of the model leads to error propagations e.g. the surface measurement errors. In [40, 15] the authors reconstruct the surface elevation  $H$  and the bed elevation  $b$  from the surface velocity  $\mathbf{u}_H$  and depth measurements given at upstream again. The inversions are based on the traditional SIA equation and velocity expression i.e. with no-slip at bottom only. This limits the applicability of the approach. Similarly [27] infers the topography of non-sliding mountain glaciers from the surface elevation data  $H$  (and mass-balance  $a$ ). Again, since the direct model is a non-linear transport equation (the inverse problem aims at inverting the divergence operator), the authors solve a pseudo-time dependent problem and introduce artificial diffusion to regularize the first order operator. Let us point out that the introduction of artificial diffusion to invert the divergence operator presents serious drawbacks: the inverse problem is not the original one and the computed solution is fully dependent on the regularization parameter. Also, the inversion is highly unstable or even numerically impossible, depending on the locations of the measurements at boundaries. Roughly, only data in the vicinity of a characteristics root can be inferred (roughly for a given flow line, this corresponds to the inflow data). In the unsteady case, the authors of [27] point out that smoothing the surface data is mandatory, then the computed solution is fully dependent on this additional regularization parameter. Next the same authors developed a so-called “shape optimization” approach, see [28] (actually it is a parameter identification method since it aims at identifying the

model parameter  $b$  while the domain shape is fixed). The problem is formulated as a classical optimal control problem solved by VDA, leading to a more robust than the algorithms presented in [27]. Let us point that such a straightforward “blind” VDA may be unable to infer the bottom properties in presence of the additional unknown: the spatially distributed friction parameter  $C(x, t)$ . Indeed in this case, equifinality issues can appear as demonstrated in different ways and in different contexts in [11, 13][41][16],[26, 25] [7]. Other studies address the topography inference but either in 1D only (following flow-lines) and/or based on empirical flux estimations, see e.g. [17].

All the aforementioned existing methods, excepted [41], are either based on the regularization of a transport equation (hence presenting drawbacks and limitations) and/or consider the inference of the topography only. The inverse method of [41] is based on the perturbation theory developed in [11] hence small variations of the inferred quantity ( $b, C$ ) only can be inferred, moreover for fast ice streams only (in this case, the bed-to-surface transfer function is much less filtered compared to sheared flows).

The present study aims at inferring the *complete bottom properties i.e. the (topography  $b$ , friction  $C$ ) pair in a multi-regime shallow ice flow* (hence presenting local and extremely stiff variations of the friction parameter  $C$ ) without any artificial regularization nor particular measurement location requirements (like it is the case if inverting the first order divergence operator). Since the model considered is the SIA model (more precisely the so-called extended SIA equation denoted xSIA), the method domain of validity ranges from fully sheared to mildly sheared flows hence valid for a large panel of observed ice flows (however this excludes the fast ice-streams since unsheared and not properly modeled by the SIA models).

The present method guideline is to consider intrinsically invertible equations only (typically diffusive / parabolic-elliptic second order equations and not first order equations), and to consider robust, well-posed optimal control problems only. The goal has been reached by basing the inverse method on a combination of explicit field expressions of the xSIA equation *and* an intermediate linear-quadratic optimal control problem (hence well-posed); the latter is classically solved by VDA.

The required measurements are the surface elevation  $H$  and the surface velocity norm  $|\mathbf{u}_H|$  plus some in-situ depth measurements. The latter can be located anywhere relatively to the stream lines. The strengths of the resulting inversion method are the following:

i) A high robustness, including in presence of uncertain surface measurements and whatever the depth measurements locations;

ii) A large domain of validity in terms of flow regimes: from fully sheared to mildly sheared flows. Thus it can be applied to the great majority of the ice-sheet surfaces (corresponding to the accumulation areas) and high-mountains glaciers; but this excludes the fast ice-streams. (However for fast ice-stream in coastal ice sheet areas, the depth-mass equation inversion can be efficient, see [34, 35, 33]).

iii) A capability to infer separately the depth from the spatially distributed friction coefficient  $C$ . The inference of  $C$  becomes a by-product of the depth inference. This feature is important since potential equifinality issues while identifying the pair (topography, friction). Also the friction coefficient is one of the greatest uncertain parameter in geophysical shallow flow models, its values vary within few orders of magnitudes and its estimation by expert assessment is generally impossible.

Finally a by-product of the present analysis is a methodology to define consistent slope scales in SIA models.

Since based on shallow flow equations, this inverse method remains affordable even for large computational domains (e.g. the whole ice-sheets); this is particular true if the VDA process is implemented in parallel like it can be done in DassFlow [30] or ISSM [21] for example. The present numerical results have been performed by using the Fenics Python library [1, 23].

The weakness of the method is its relative inaccuracy in the narrow regime transition areas like canyon margins. This gives local error peaks (of 20-30% approx.), corresponding to the stiff variations of the inferred quantities (variations extremely local and of few orders of magnitude like the friction coefficient).

The outline of the article is as follows. In Section 2, the classical SIA equation and field expressions are re-derived; then clarifying their respective domain of validity in terms of basal friction amount (or equivalently in terms of the slip ratio  $R_s$ ). This leads to the definition of three sub-regimes corresponding to different slip ratio range values. Next the definition and derivation of additional expressions are presented. Section 3 describes the complete inference method. For each sub-regime, an explicit expression of the depth  $h$  is derived; all of them depend on a unique observational surface term denoted  $Q_H$ . For two sub-regimes, the depth expression depends on the “diffusivity”  $\eta$  of the xSIA equation. This diffusivity is numerically computed by VDA. Finally, the friction coefficient value  $C$  can be explicitly deduced. Next, the complete method is assessed on academic test cases presenting the complete range of flow regimes with stiff transition areas (hence presenting many difficulties of real-world flows). The multi-regime academic test case is constructed in Section 4. A method to define an a-priori slip ratio map, next a good depth first guess is developed. Section 5 aims at analysing the numerical results in the case of downstream depth measurements, both for perfect and uncertain surface measurements. Various sensitivity analysis (explicit and numerical ones) are highlighted and commented. An extra difficult test case based on lateral depth measurements only (measurements quasi parallel to a flow line, moreover within a

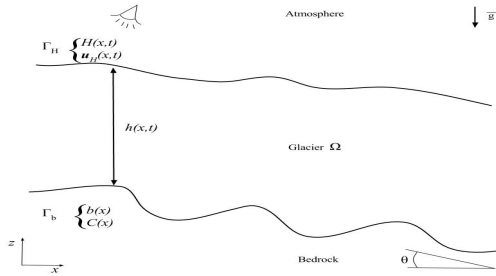


Figure 1: Notations. A shallow ice flow ( $x$ - $z$  view) along an inclined mean slope, with surface observations.

mono-regime area) is analysed in Section 6. Finally, it turns out that the few depth estimations aforementioned  
 165 make possible to determine the correct slope scale in a SIA model. This is explained how and illustrated for 1D  
 uniform flows in Section 7. The conclusion proposes few perspectives of this preliminary study.

## 2 The direct model

In this section, the direct model and various explicit field expressions are derived. As a first step, the classical  
 170 Shallow Ice Approximation (SIA) velocity expression and resulting equation are re-derived, see [18], [31], see  
 also e.g. [5] chapter 10.2. The SIA equations derive following standard asymptotical calculations of the free  
 surface (non-linear) Stokes equations with respect to the geometrical ratio  $\varepsilon = \frac{H^*}{L^*}$ ; with  $H^*$  a characteric flow  
 depth and  $L^*$  a characteric flow length. The basic assumption states that the flow, thin geometry, is sheared;  
 in other words, the normal stress components are negligible. The order 0 SIA equations are in fact order 1 in  
 175  $\varepsilon$ . In the literature “SIA model” generally denotes the no-slip case at bottom (fully sheared flow); also this  
 terminology denotes indistinctly the explicit velocity expressions (derived from the momentum equations only)  
 and the corresponding lubrication type equation (derived from the depth-averaged mass equation). A much  
 less employed SIA equation is obtained if considering a non vanishing velocity at bottom, see e.g. [5] chapter  
 10.2 or [10]chapter 5.4. For a sake of precision, in this article this less classical version of the equations is called  
 180 extended (xSIA). In [3], it is formally demonstrated that the xSIA model remains valid for a friction coefficient  
 $C \simeq \mathcal{O}(1)$ , hence clarifying the xSIA domain of validity. This legitimates the few sub-regimes considered in next  
 section. (In [3], the xSIA equation is a particular case of more general shallow flow models, see Section 11 of this  
 reference). In other respect, in the literature the xSIA equation is derived in the mean slope coordinate system  
 (otherwise in the horizontal-vertical coordinate system). Nevertheless it is demonstrated in [3] that the same  
 185 expressions and equation remain valid in a more general coordinate system: the Prandtl coordinate system.  
 Then this makes possible to apply the model to any bottom shape (i.e. without any clear mean slope) like those  
 observed in some high mountains glaciers for example.

In summary, the xSIA equation and field expressions derived below are valid for any coordinate system (here  
 presented in the mean slope coordinate system for a sake of clarity), non-isothermal flows and flows from fully  
 190 sheared (no slip,  $C = 0$ ) to mildly sheared ( $C \simeq \mathcal{O}(1)$ ). Next, various additional explicit expressions are derived;  
 the latter being important in the forthcoming inversion method.

### 2.1 Basic notations and rheology

We denote by  $H$  the fluid elevation,  $b$  the topography elevation,  $h = (H - b)$  the fluid depth, see Fig. 1.

The gravity is denoted by  $g$ , the fluid density by  $\rho$ ; the 3D fluid velocity is denoted by  $\mathbf{U} = (u, v, w) = (\mathbf{u}, w)$   
 195 and its pressure by  $p$ . The stress tensor is denoted by  $\sigma$ :  $\sigma(\mathbf{U}) = \tau(\mathbf{U}) - p\mathcal{I} = 2\mu D(\mathbf{U}) - p\mathcal{I}$ ; with  $\mu$  the  
 viscosity and  $D$  the symmetric rate of strain tensor,  $D(\mathbf{U}) = \frac{1}{2} (\nabla\mathbf{U} + (\nabla\mathbf{U})^T)$ . For a sake of simplicity in the  
 forthcoming expressions, it is assumed that the geometry presents a “mean slope” in the  $(x, y)$ -axis which can  
 be described by the angle  $\theta$ . Then,  $\mathbf{g} = (g \sin \theta, 0, -g \cos \theta)^T$ , Fig. 1.

**Rheology law.** The ice rheology is a power-law (generalized Newtonian fluids). Then the deviatoric stress  
 tensor reads :  $\tau = 2\mu D(\mathbf{U}) = 2\mu_0 \dot{\gamma}^{n-1} D(\mathbf{U})$ .  $\dot{\gamma}$  is the effective strain rate defined by:  $\dot{\gamma} = \frac{1}{\sqrt{2}} \|D(\mathbf{U})\|_F$   
 (Frobenius norm of the strain rate), and the viscosity  $\mu = \mu_0 \dot{\gamma}^{n-1}$  is a power-law of the effective strain rate;  $\mu_0$   
 200 is the consistency. The power-law exponent  $n \in ]0, 1[$  for shear thinning fluids: ice but also lava, mud and many  
 industrial fluids. Recall that  $n > 1$  for shear thickening fluids (less common fluids) and  $n = 1$  for Newtonian  
 205 fluids.

*Invert rheology law.* By defining the effective stress:  $\tau_e = \frac{1}{\sqrt{2}} \|\tau\|_F = 2\mu_0 \dot{\gamma}^n$ , the so-called Nye-Glen-Steinmann's flow law follows:  $D(\mathbf{U}) = A\tau_e^{q-1}\tau$  with the exponent  $q = \frac{1}{n}$ .  $A$  is the rate factor,  $A = \frac{1}{(2\mu_0)^q}$ .

For glaciers, the usual exponent value is  $q = 3$ . Also for glaciers, the consistency  $\mu_0$  and the rate factor  $A$  depend on the temperature field.

210 In the present study,  $A$  (or equivalently  $\mu_0$ ) is assumed to be given but depending on the space variables, in particular on the depth variable  $z$ .

## 2.2 Boundary conditions

Given a boundary of the geometrical domain  $\Omega$ ,  $\mathbf{n}$  denotes its outward normal and  $(\mathbf{t}^{(1)}, \mathbf{t}^{(2)})$  denotes its tangential vectors with  $(n, \mathbf{t}^{(1)}, \mathbf{t}^{(2)})$  direct.

215 The free-surface (interface fluid-atmosphere) is denoted by  $\Gamma_H$ ,  $\Gamma_H = \{(x, y, z) \in \mathbb{R}^3 | z = H(x, y)\}$ . On  $\Gamma_H$ , the ice stress condition reads:  $(\tau - p\mathcal{I})\mathbf{n} = 0$ .

Furthermore, the free surface dynamics reads:

$$\partial_t H + \mathbf{U}_H \nabla H = a \quad (1)$$

with  $a$  the mass balance (between accumulation and ablation).

220 The bottom boundary  $\Gamma_b$  is defined by:  $\Gamma_b = \{(x, y, z) \in \mathbb{R}^3 | z = b(x, y)\}$ . On  $\Gamma_b$ , a friction power-law is imposed; it models the till interface as a viscous boundary layer.

The basal shear stress reads:  $\tau_b = \tau \cdot \mathbf{n} - (\mathbf{n}^T \cdot \tau \cdot \mathbf{n}) \cdot \mathbf{n}$ ; the tangential velocity vector reads:  $\mathbf{u}_b = (u_b, v_b) = \mathbf{U} - (\mathbf{n}^T \cdot \mathbf{U}) \cdot \mathbf{n}$ . The classical non-linear Weertman-type friction law is imposed:

$$(u_b, v_b) = C |\tau_b|^{q-1} (\tau_{xz}, \tau_{yz}) \text{ and } w_b = (u_b, v_b) \cdot \nabla b$$

For a sake of simplicity, the law exponent is chosen equal to the rheology one; typically  $q = 3$ .

225 The coefficient  $C$  is the slip coefficient. If  $C \rightarrow 0$ , the no-slip condition (adherence) is imposed; on the contrary if  $C \rightarrow \infty$  a pure slip condition (vanishing friction) is imposed. Nevertheless, to remain within the SIA model validity, the slip coefficient  $C$  has to vary from 0 to  $\mathcal{O}(1)$  at most, see e.g. [3] for a detailed discussion and analysis.

## 2.3 The mass equation and explicit velocity expressions

230 The depth averaged velocity  $\bar{\mathbf{u}}$  and the discharge  $\mathbf{q}$  are defined by:

$$\bar{\mathbf{u}} = \frac{1}{h} \int_b^H \mathbf{u}(z) dz \text{ and } \mathbf{q} = h\bar{\mathbf{u}} = h(\bar{u}, \bar{v}) \quad (2)$$

The bottom topography is assumed to be time independent. By integrating the 3D incompressibility equation  $div(\mathbf{u}) = 0$ , by using the Leibnitz integration rule and the free surface dynamics equation (1), the depth averaged mass equation is obtained:

$$\partial_t h + div_{xy}(\mathbf{q}) = a \quad (3)$$

235 Momentum equations. The 3D Stokes equations, 0th order in the geometrical ratio  $\varepsilon = \frac{H}{L}$ , are integrated in  $z$ ; it gives:

$$(\tau_{xz}, \tau_{yz}) = (H - z)(S_x, S_y) = (H - z)\mathbf{S} \quad (4)$$

with  $\mathbf{S} = \nabla H$  the free surface slope, see e.g. [5, 3]. Then the shear tensor at bottom reads:  $\tau_b = (\tau_{xz}, \tau_{yz})|_b = \mathbf{S}h$ . The third momentum equation gives the hydrostatic pressure expression:  $p(z) = (H - z)$ . The incompressibility condition gives:  $\tau_{zz} = -(\tau_{xx} + \tau_{yy})$ .

240 The effective stress reads:  $\tau_e = |\mathbf{S}|(H - z)$ . Next the velocity derivatives expressions derive from the rheology equations:

$$\begin{cases} \partial_x u & = A\tau_e^{q-1}\tau_{xx} \\ \frac{1}{2}(\partial_y u + \partial_x v) & = A\tau_e^{q-1}\tau_{xy} \\ \frac{1}{2}(\partial_z u + \partial_x w) & = A\tau_e^{q-1}\tau_{xz} \\ \partial_z w & = A\tau_e^{q-1}\tau_{zz} \end{cases} \quad (5)$$

with similar expressions for  $\partial_y v$  and  $\frac{1}{2}(\partial_z v + \partial_y w)$ . Recall that  $A$  is the rate factor. Let us define:

$$\mathcal{S} = |\mathbf{S}| = |\nabla H| \text{ and } \bar{\rho} = (\rho g \cos \theta)^q \quad (6)$$

By integrating in  $z$  between  $b$  and  $z$  the expressions of  $\partial_z(u, v)$ , the longitudinal velocity components follow:  $\mathbf{u}(z) = (u, v)(z) = \mathbf{u}_b + 2\bar{\rho}\mathcal{S}^{q-1}\mathbf{S} \int_b^z A(H - \xi)^q d\xi$ . This is the classical SIA velocity expressions. They are presented in the isothermal case for example in [5] chapter 10.2, or in [10] chapter 5.4 in the horizontal-vertical coordinate system ( $\theta = 0$ ) with  $u_b = 0$  (no slip at bottom).

*Remark 1.* The rate factor  $A$  hence the viscosity  $\mu_0$  a-priori depend on  $z$ . In the case  $A$  independent on  $z$  (isothermal case), it follows:  $\mathbf{u}(z) = \mathbf{u}_b + \frac{2A}{(q+1)}(\rho g \cos \theta)^q |\mathbf{S}|^{q-1} [h^{q+1} - (H - z)^{q+1}] \mathbf{S}$ .

Furthermore using the boundary conditions at bottom, it follows:  $\mathbf{u}_b = C(\rho g \cos \theta)^q h^q |\mathbf{S}|^{q-1} \mathbf{S}$ . Then the longitudinal velocity reads:

$$\mathbf{u}(z) = (u, v)(z) = \bar{\rho} [Ch^q + 2 \int_b^z A(H - \xi)^q d\xi] \mathcal{S}^{q-1} \mathbf{S} \quad (7)$$

Note that the vertical velocity field  $w$  can be recovered from the incompressibility equation:  $w(z) = (u_b, v_b) \cdot \nabla b - \int_b^z (\partial_x u + \partial_y v) dz$ .

A validity analysis of this velocity expression (7) in terms of flow regime (defined from the friction parameter  $C$  range value) is presented in [3]. This is closely related to the slip ratio defined below.

In order to obtain a direct expression of  $\mathbf{u} = (u, v)$  (without the integrals), the rate factor  $A$  has to be independent of  $z$ .

## 2.4 Additional explicit expressions and definitions

An explicit expression of the depth averaged velocity  $\bar{u}$  can be derived. To do so, let us define  $\bar{A}$  independent of  $z$  by:  $\bar{A} = \int_b^H \int_b^z (H - \xi)^q d\xi dz = \int_b^H \int_b^z A(H - \xi)^q d\xi dz$ , hence:

$$\bar{A} = \frac{q+2}{h^{q+2}} \int_b^H \int_b^z A(H - \xi)^q d\xi dz \text{ for all } (x, y; t) \quad (8)$$

Given  $A(z)$  (typically in the thermal dependent case), the quantity  $\bar{A}$  can be computed numerically for each  $(x, y; t)$ . Then the depth averaged velocity reads:

$$\bar{\mathbf{u}} = \bar{\rho} [C + \frac{2\bar{A}}{(q+2)} h] h^q \mathcal{S}^{q-1} \mathbf{S} \quad (9)$$

Similarly, an explicit expression of the surface velocity  $\mathbf{u}_H$  can be derived. To do so, let us define  $\underline{A}$  as follows:  $\int_b^H A(H - \xi)^q d\xi = \underline{A} \int_b^H (H - \xi)^q d\xi$ . Hence:

$$\underline{A} = \frac{q+1}{h^{q+1}} \int_b^H A(H - \xi)^q d\xi \text{ for all } (x, y; t) \quad (10)$$

Then the surface velocity  $\mathbf{u}_H$  reads:

$$\mathbf{u}_H = \bar{\rho} [C + \frac{2A}{(q+1)} h] h^q \mathcal{S}^{q-1} \mathbf{S} = \mathbf{u}_b + \frac{2\bar{\rho}\underline{A}}{(q+1)} h^{q+1} \mathcal{S}^{q-1} \mathbf{S} \quad (11)$$

Let us point out that in the isothermal case (hence  $A$  independent on  $z$ ),  $\bar{A} = \underline{A} = A$ . Finally let us define the slip ratio as follows:

$$R_s = \frac{|\mathbf{u}_H| - |\mathbf{u}_b|}{|\mathbf{u}_H|} = 1 - \frac{|\mathbf{u}_b|}{|\mathbf{u}_H|} = 1 - \frac{C}{[C + \frac{2A}{(q+1)} h]} = \frac{\frac{2A}{(q+1)} h}{[C + \frac{2A}{(q+1)} h]} \quad (12)$$

The slip ratio  $R_s$  equals 1 for fully sheared flow (sub-regime 1) and equals 0 for plug like flow.

The case  $R_s = 0$  is out of the validity range of the present Shallow Ice Approximation validity since the scalings assumed to derive the velocity expressions above are not valid anymore. The present SIA equations are a-priori valid up to a slip ratio  $R_s \approx 0.5$  since the basic scaling done in the SIA equations make possible the asymptotic derivations up to a balance between  $C$  and the term  $\frac{2A}{(q+1)} h$ , see [38, 3] for a more detailed discussion on this point.

Note that  $R_s = 0.5$  is equivalent to the equality:  $C = \frac{2A}{(q+1)} h$ .

## 2.5 The xSIA equation

By injecting the discharge expression  $\bar{\mathbf{q}} = h\bar{\mathbf{u}}$  with (9) into the free surface dynamics equation, an one-equation model (lubrication type) is obtained; it is the xSIA equation.

$$\partial_t h - \bar{\rho} \operatorname{div}_{xy} \left( \left[ C + \frac{2\bar{A}}{(q+2)} h \right] h^{q+1} \mathcal{S}^{q-1} \nabla H \right) = a \quad (13)$$

with  $\mathcal{S} = |\nabla H|$ ,  $q \geq 1$ . This non linear parabolic model has to be closed with boundary conditions (Dirichlet or Neumann conditions on  $H$ ) and initial conditions.

**Steady-state version.** In a glacier modeling context, uncertainties on the mass source term  $a$  (modeling the ablation / deposition at the surface) may be of the same order than the time variation  $\partial_t h$ . (This depends of course on the considered time scale and/or the flow). Then it is classical to consider the effective source term:  $\dot{a} = -\partial_t h + a$ .

Then the steady-state version of the xSIA equation reads:

$$-\bar{\rho} \operatorname{div}_{xy} (\eta(C, h) \mathcal{S}^{q-1} \nabla H) = \dot{a} \quad (14)$$

where  $\eta$  denotes the “effective diffusivity”:

$$\eta(C, h) = \left[ C + \frac{2\bar{A}}{(q+2)} h \right] h^{q+1} \quad (15)$$

This non linear elliptic equation has to be closed with boundary conditions on  $H$  (Dirichlet conditions or mixed ones).

*Remark 2.* Under the assumption the diffusivity  $\eta(C, h)$  is given, if the surface slope  $\mathcal{S}$  is given too (surface measurements), then the equation (14) is a gentle linear elliptic equation. Nevertheless, it is well-known and easily verified that its solution  $H$  is highly sensitive to the definition scale of the slopes  $\mathbf{S}$ . This feature is addressed in the last section.

## 3 Inference of the (topography, friction) pair from the surface measurements ( $\mathcal{S}, \mathbf{u}_H$ )

In this section the complete inference method is derived into details; it is assessed on academic test cases in next sections. First the inverse problem is presented and the different sub-regimes are introduced: fully sheared flow, mildly sheared flow and weakly sheared flow. The slip ratio criteria, measuring the regime type, is defined. Next the observational surface term  $\mathcal{Q}_H$  is naturally defined from the surface observations: elevation  $H$  and velocity norm  $\mathbf{u}_H$ . Next the central three depth estimations, corresponding to the three sub-regimes, are derived.

In the sub-regime 1 case, the depth estimation is directly obtained from the observational term  $\mathcal{Q}_H$ . In the sub-regime 3 case, the depth estimation is explicit but depends on an intermediate variable  $\eta$ : the “effective diffusivity” of the xSIA equation, see (14).  $\eta$  can be inferred by a Variational Data Assimilation process applied to a linear version of the xSIA equation, hence aiming at solving a well-posed linear-quadratic control problem. Finally the intermediate and most general case (it includes the two others cases), is the mildly sheared case (sub-regime 2). In that case, the depth can be inferred as a root of a polynomial which depends on the variable  $\eta$ .

Next, it is demonstrated that the friction coefficient  $C$  is a simple by-product of the depth estimations above; its explicit expressions are derived. Hence the present approach makes possible the inference of the bed topography  $b$  separately of the the friction coefficient  $C$ . This is a crucial feature of the method and an indication of its robustness.

Finally the VDA process aiming at identifying the effective diffusivity  $\eta$  is detailed: the adjoint equations and the gradient cost function used to solve numerically the optimal control problem are detailed.

### 3.1 The inverse problem and the observed surface term $\mathcal{Q}_H$

The direct problem reads as follows: given the basal properties (topography, friction coefficient)  $(b, C)$ , find  $H$  solution of (14)(15), accompanied with boundary conditions. Then the depth  $h = (H - b)$  is straightforwardly deduced.

The considered inverse problem reads as follows: *given the surface observations*  $(\mathbf{H}, \mathcal{S}, \mathbf{u}_H)$ , *find the pair*  $(h, C)$ .

In the next paragraph, explicit expression of the depth  $h$ , than  $C$ , are derived in function of an unique observed quantity, and potentially in function of the effective diffusivity  $\eta$  defined by (15). To do so, three sub-regimes are considered.

### The three sub-regimes: from fully sheared to pure slip

Let us define the considered three sub-regimes.

- Sub-regime 1 (sr1): the fully-sheared sub-regime which corresponds to a vanishing friction coefficient. Then  $C$  is set to 0. This sub-regime 1 corresponds to the slip ratio  $R_s$  tends to 0.
- Sub-regime 2 (sr2): the mildly-sheared regime in the sense  $C \approx Ah$ . Typically, let us recall that  $R_s = 0.5$  corresponds to  $(q + 1)C = 2Ah$ .
- Sub-regime 3 (sr3): the weakly sheared regime in the sense  $C \gg Ah$ , hence the slip ratio  $R_s$  tends to 1.

Let us point out that all forthcoming derivations made in the intermediate regime (mildly sheared, sub-regime 2) are valid in the two other extreme sub-regimes (sub-regimes 1 and 3).

A formal error estimate of the asymptotic xSIA equation presented in [3] demonstrates that sub-regime 2 is the limit case of the xSIA equation validity. In other words for  $C$  larger, the a-priori scaling made to obtain the xSIA equation breaks down. Indeed, this a-priori scaling (roughly  $\sigma_{xz} \gg \sigma_{xx}$ ) is not valid anymore in the sub-regime 3, see [38] too. Nevertheless, it will turned out that the depth estimates obtained but assuming  $C \gg Ah$  (sub-regime 3 case) is a particular case of those obtained in the sub-regime 2 case.

All the estimates derived in this section will be assessed in next section on an academic test case presenting the full range of flow regime (i.e. the full range of slip ratio).

**The observational surface term  $\mathcal{Q}_H$**  The surface quantity which naturally appears in the expressions above is the ratio between the surface velocity norm and the surface slope norm:

$$\mathcal{Q}_H = \frac{|\mathbf{u}_H|}{S^q} \quad (16)$$

Finally let notice that the slip ratio  $R_s$  defined by (12) can be read in function of  $\mathcal{Q}_H$  (and the depth  $h$ ) as follows:

$$R_s = \frac{2\bar{\rho}A}{(q+1)} \frac{h^{q+1}}{\mathcal{Q}_H} \quad (17)$$

### 3.2 Sub-regime 1 (fully sheared): explicit expression of $h$

Let us consider a vanishing friction coefficient  $C$ . It follows the usual SIA expression of  $\mathbf{u}_H$ :

$$\mathbf{u}_H = \frac{2\bar{\rho}A}{(q+1)} \mathcal{S}^{q-1} \mathbf{S} h^{q+1} \quad (18)$$

Then from the surface measurements  $(\mathbf{u}_H, \mathcal{S})$ , the depth  $h$  can be straightforwardly estimated by:

$$h \approx \left[ \frac{(q+1)}{2\bar{\rho}A} \mathcal{Q}_H \right]^{1/(q+1)} \equiv h_{sr1} \quad (19)$$

Note that this depth estimate does not depend on the vectorial features of the surface measurements; it depends on norms only.

Let us recall that sub-regime 1 corresponds to the “traditional SIA regime” and few studies has addressed the depth inversion in this case, see the general introduction. The forthcoming numerical results demonstrate that the present estimation is not accurate as soon as the slip ratio is lower than  $\approx 0.85$ .

### 3.3 The general expression: sub-regime 2 case

Sub-regime 2 corresponds to a mildly sheared regime, hence much faster flows than sub-regime 1. Nevertheless, this sub-regime still corresponds to the xSIA model validity (see [3] for a detailed analysis). The typical case is  $R_{slip} = 0.5$  or equivalently :  $(q+1)C = 2Ah$ . Some depth expressions (explicit or not) are derived. Also, it will turn out that by considering the two terms in the analytical expressions (the slip term and the deformation term), the depth derivations below remain valid for all sub-regimes.

### 3.3.1 Algebraic system in $(h, C)$

Given the surface quantity  $\mathcal{Q}_H$  (from the surface velocity and slope measurements), by using the surface velocity expression (11), it follows:

$$[C + \frac{2}{q+1}\underline{A}h]h^q = \frac{\mathcal{Q}_H}{\bar{\rho}} \quad (20)$$

This expression combined with the expression of the effective diffusivity  $\eta$ , see (15), leads to the following non linear algebraic system in  $(h, C)$ :

$$\begin{cases} [C + \frac{2}{q+1}\underline{A}h]h^q = \frac{\mathcal{Q}_H}{\bar{\rho}} \\ [C + \frac{2}{q+2}\bar{A}h]h^{q+1} = \eta \end{cases} \quad (21)$$

Let us point out that these two equations are *not* redundant. Indeed, the surface velocity expression is based on the momentum equation only while the xSIA equation (14) includes in addition the depth mass equation.

In a discrete point of view, if denoting by  $N$  the number of the degree of freedom of each field (e.g. the Finite Element degrees of freedom), then (21) is a  $2N$  equations with  $2N$  unknowns (the  $N$  pairs  $(h, C)$  pairs).

### 3.3.2 Polynomial in $h$

By injecting the first equation (the observed surface expression) into the second one (the effective diffusivity expression), it follows the following polynomial in  $h$ :

$$a_2 h^{q+2} - \frac{\mathcal{Q}_H}{\bar{\rho}} h + \eta = 0 \quad (22)$$

with:  $a_2 = m[(q+2)\underline{A} - (q+1)\bar{A}]$  and  $m = \frac{2}{(q+1)(q+2)}$ .

In the isothermal case  $a_2 = mA$ . Also observe that for  $q = 3$ , the polynomial is order 5, with  $m = \frac{1}{10}$ .

Given  $\eta$ , and the observed quantity  $\mathcal{Q}_H$ , the depth  $h_{sr,2}$  can be inferred by computing the roots of polynomial (22). It is classically done by computing the eigenvalues of the companion matrix.

*Remark 3.* In the isothermal case, this polynomial expression gives:  $\frac{\mathcal{Q}_H}{\bar{\rho}} (\frac{R_s}{(q+2)} - 1)h + \eta = 0$  with  $R_s$  the slip ratio defined by (17). Hence the depth expression in the sub-regime 2 case:

$$h = \left[1 - \frac{R_s}{(q+2)}\right]^{-1} \frac{\bar{\rho}}{\mathcal{Q}_H} \eta \equiv h_{sr,2} \quad (23)$$

Even if  $\eta$  is given, this explicit expression cannot be evaluated in practice since the slip ratio  $R_s$  is a-priori unknown. Nevertheless, in the sequel this expression is useful, in particular to analyse the depth estimate sensitivity with respect to the variations of  $\mathcal{Q}_H$ .

*Remark 4.* The depth expression (23) includes the sub-regime 1 case. Indeed, if setting  $R_s = 1$  and  $C = 0$  in the  $\eta$  expression, it follows:  $h^{q+1} = \frac{(q+1)}{2\bar{\rho}A} \mathcal{Q}_H$ . This is nothing else than (19) in the isothermal case.

## 3.4 The sub-regime 3 case

In the case of sub-regime 3,  $Ah$  is negligible compared to  $C$ , then the algebraic system (21) simplifies as follows:

$$\begin{cases} Ch^q \approx \frac{1}{\bar{\rho}} \mathcal{Q}_H \\ Ch^{q+1} \approx \eta \end{cases} \quad (24)$$

and it follows straightforwardly the depth expression:

$$h \approx \frac{\bar{\rho}}{\mathcal{Q}_H} \eta \equiv h_{sr,3} \quad (25)$$

Given  $\eta$ , and the observed quantity  $\mathcal{Q}_H$ , the depth  $h$  can be straightforwardly inferred.

Equivalently, the depth expression (23) which is obviously valid in the sub-regime 3 case, leads directly to (25) by making vanish the slip ratio  $R_s$ . In other words, the sub-regime 3 is a sub-case of the sub-regime 2 case. Finally the intermediate case include all the others and the sub-regime 2 estimations above are the most general ones.

In next section, it will be presented how the diffusivity  $\eta$  can be approximated by Variational Data Assimilation (VDA), hence making possible the depth estimations in sub-regime 2 and sub-regime 3.

*Remark 5.* Let us calculate the difference between the two extreme estimations (19) and (25). For a sake of simplicity, the flow is supposed to be isothermal ( $\bar{A} = \underline{A} = A$ ). From (19), it follows:  $\frac{\mathcal{Q}_H}{\bar{\rho}} = \frac{2A}{(q+1)} h_{sr1}^{q+1}$ . While from (25), it follows:  $\frac{\mathcal{Q}_H}{\bar{\rho}} = \frac{\eta}{h_{sr3}}$ .

If setting  $C = 0$  in  $\eta$  in the sub-regime3 depth estimation (25), it follows:  $\frac{2A}{(q+1)} h_{sr1}^{q+1} = \frac{1}{h_{sr3}} \cdot \frac{2A}{(q+2)} h_{sr1}^{q+2}$ .

400 Hence:  $h_{sr3} = \frac{(q+1)}{(q+2)} h_{sr1}$ .

In others words, given the  $\eta$  value in the fully sheared areas ( $R_s$  close to 1), the depth formula corresponding to the vanishing slip ratio gives a value  $\frac{(q+1)}{(q+2)}$  smaller than the true one (hence 20% smaller in the case  $q = 3$ ). Nevertheless, it will be noticed in the forthcoming test case that the value range of  $\eta$  is very large (few orders of magnitudes) hence leading to differences of depth much greater than the present 20%. Nevertheless, this  
405 remark will be useful to select the correct computed polynomial root of (22).

### 3.5 The resulting friction coefficient $C$

Given the depth value  $h$ , whatever in sub-regime 1, 2 or 3, the corresponding friction coefficient value  $C$  can be deduced from (21). Its value can be deduced equivalently from the first equation:

$$C = \frac{1}{\bar{\rho} h^q} \mathcal{Q}_H - \frac{2}{(q+1)} \bar{A} h, \quad (26)$$

or from the second equation:

$$C = \frac{\eta}{h^{(q+1)}} - \frac{2}{q+2} \bar{A} h \quad (27)$$

410 Since the observed surface term is uncertain, since the VDA process to compute  $\eta$  is not exact (see next paragraph), a-priori these two equations may give very slightly different friction values. Nevertheless in the numerical experiments presented in next section, both expressions give extremely close values for  $C$ .

## 3.6 Identification of the effective diffusivity $\eta$ by Variational Data Assimilation (VDA)

### 415 3.6.1 Set up of the VDA problem

The depth estimates in sub-regimes 2 and 3 are based on the assumption that the effective diffusivity  $\eta$  defined by (15) is given. This quantity  $\eta$  can effectively be computed by solving a linear-quadratic optimal control problem. Indeed, let us recall that the direct model reads as follows, see (14):

$$-\bar{\rho} \operatorname{div}_{xy}(\eta(C, h) \mathcal{S}^{q-1} \nabla H) = \dot{a} \quad (28)$$

plus boundary conditions. It is a linear elliptic equation in  $H$ . Then the typical observation function is  
420 defined by:  $J(\eta; H) = \frac{\alpha_H}{2} \int_{\Omega} (H^\eta - H^{obs})^2 dx + \frac{\alpha_\eta}{2} \int_{\Omega} |\nabla \eta|^2 dx$ . And the cost function reads:  $\bar{j}(\eta) = J(\eta; H^\eta)$  where  $H^\eta$  is the unique solution of the linear equation (15), given  $\eta$ .

Then, given the surface measurements elevation - slope  $(H, \mathcal{S})$ , the spatially distributed coefficient  $\eta$  can be inferred by solving the optimal control problem:  $\min_{\eta} j(\eta)$ .

425 Since this optimal control problem is linear quadratic then it admits an unique optimal solution  $\eta^*$ .

In practice, it turns out that the quantity  $\eta$  varies greatly ( $\approx 4$  orders of magnitude in a multi-regime flow), then a log change of variable is introduced; the control variable becomes  $\omega = \ln(\eta)$ . Furthermore the power of the regularizing term is increased. (The regularizing process has been observed to be more efficient with the  $L^4$   
430 norm than with the  $L^2$  norm). The minimized cost function reads:

$$j(\omega) = \frac{1}{2} \int_{\Omega} (H^\omega - H^{obs})^2 dx + \frac{\alpha_\omega}{2} \int_{\Omega} |\nabla \omega|^4 dx \quad (29)$$

with  $\alpha_\omega$  to be set. And the optimal control problem reads:

$$\min_{\omega} j(\omega) \quad (30)$$

Let us point out that (30) is no longer a linear-quadratic optimal control problem (the cost function is not quadratic anymore due to the log change of variables), but the cost function remains strictly convex and the inverse problem still admits an unique optimal solution  $\omega^*$ .

435 *Remark 6. On the impossibility to directly assimilate  $\mathbf{u}_H$  into the xSIA equation.*

The misfit between the xSIA model and the surface observations can be based on the elevation measurements  $H$  only (e.g. acquired by altimetry) and not on the surface velocities  $\mathbf{u}_H$  since the latter depends on the unknown (depth, friction) pair  $(h, C)$ , see (11). Thus observed  $\mathbf{u}_H$  (e.g. derived from InSAR) are not directly assimilated by VDA. Nevertheless  $\mathbf{u}_H$  appears in the three depth estimations through the observational term  $\mathcal{Q}_H$ , see (16) and (19)(23)(25).

The surface velocity  $\mathbf{u}_H$  (11) and the depth averaged velocity  $\bar{\mathbf{u}}$  (9) depend on  $\eta$  but also on  $(C, h)$ . Therefore the basal features  $(C, b)$  cannot be identified while identifying  $\eta$  only.

### 3.6.2 The equations and numerical methods

445 The direct model (14)-(15) is numerically solved using a standard Lagrange finite element method, by employing the Fenics Python library [1, 23]. The weak formulation consists to find  $H \in V_t$  such that:  $\forall \phi \in V_0$ ,  $a(\omega; H, \phi) = b(\phi)$  with

$$a(\omega; H, \phi) = \bar{\rho} \int_{\Omega} \mathcal{S}^{q-1} e^{\omega} \nabla H \nabla \phi \, dx \text{ and } b(\phi) = \int_{\Omega} \dot{a} \phi \, dx \quad (31)$$

and  $V_0 = W^{1,q'}(\Omega)$  an adequate Banach space ( $q'$  depending on  $q$ ,  $q \geq 1$ ),  $V_t$  its corresponding affine sub-space (taking into account the non-homogeneous Dirichlet boundary condition).

450 For  $q = 3$  and under an assumption on  $\eta = e^{\omega}$  (it has to remain bounded), the existence and uniqueness of the weak solution  $H \in V_t$  may be addressed using mathematical analysis tools of non-linear elliptic problems (variational methods and/or fixed point theorems), see e.g. [8, 9]. The detailed mathematical and finite element analysis of this equation (with extra assumptions) can be found in [20][19].

455 Next, the cost function (29) can be computed. The optimal control problem (30) is numerically solved by Variational Data Assimilation (VDA); it is based on the adjoint equations and the gradient of the cost function (first order optimization method), see e.g. [29] for details.

The adjoint equations read as follows. Given  $\omega$ , given  $H^{\omega}$  the unique solution of the state equation (31) (i.e. the direct model), find  $p^{\omega} \in V_0$  such that:  $\partial_H a(\omega; H^{\omega}, p).z = \partial_H J(\omega; H^{\omega}).z$  for all  $\forall z \in V_0$ .

Since the state equation is linear symmetric, it follows:  $\partial_H a(\omega; H, p).z = a(\omega; p, z)$ .

Also:  $\partial_H J(\omega; H^{\omega}).z = \int_{\Omega} z(H^{\omega} - H^{obs}) \, dx$ .

460 The adjoint equation can be solved by the same finite element method as the state equation.

Given the (unique) adjoint  $p^{\omega}$ , the gradient of the cost function reads, see e.g. [29] Chapter 3:

$j'(\omega) \cdot \delta\omega = \partial_{\omega} J(\omega; H^{\omega}).\delta\omega - [\partial_{\omega} a(\omega; H, p^{\omega}).\delta\omega - \partial_{\omega} b(\omega; p^{\omega}).\delta\omega] \forall \delta\omega$ , which gives:

$$j'(\omega) \cdot \delta\omega = 2\alpha_{\omega} \int_{\Omega} |\nabla\omega|^2 \nabla\omega \nabla(\delta\omega) \, dx - \bar{\rho} \int_{\Omega} \mathcal{S}^{q-1} e^{\omega} \delta\omega \nabla H^{\omega} \nabla p^{\omega} \, dx \quad \forall \delta\omega$$

465 After discretization, including of the control variable, this gives the gradient:  $\langle \nabla j, \delta\omega_h \rangle = j'(\omega_h) \cdot \delta\omega_h$ , where the index  $_h$  denotes the finite element variable. The employed minimization algorithm is the L-BFGS algorithm (quasi-Newton method, Python scipy procedure). The complete computational software has been fully assessed by implementing rigorous tests (explicit solutions with convergence curves); also the gradient computations have been compared to convergent finite difference values, see e.g. [29] Chapter 6 for details.

### 3.6.3 The complete VDA process

In all the sequel the complete VDA process is performed in two stages:

- 470 • A first one (VDA#1) by making fit the model output with the measured surface elevations only, i.e.  $\alpha_{\omega} = 0$  in (29).
- A second one (VDA#2), starting from the VDA#1 solution and by minimizing (29) with  $\alpha_{\omega}$  empirically tuned “at best”. The goal is to make a balance between the data misfit and the regularized solution (in particular in presence of noise in data).

475 Typical behaviors of both  $j$  and  $\nabla j$  vs the minimization iterations are presented in Fig. 8.

*Twin experiments.* In the present study, only synthetic data are considered, then the VDA experiments are twin experiments. The latter consist to first generate the data by running the direct model. Next, potential noise is added or not, depending on the experiment goal. Then the goal is to infer the sought quantities by the inverse method and compare the computed quantities with the original - true ones.

480 A crucial point will be to define good first guesses: both for  $(\eta, \omega)$  but also for the depth  $h$ . This crucial step will be done by employing the analytical derivations presented in the previous section.

485 *Stopping criteria.* Few classical criteria has to be evaluated before deciding the minimization algorithm has converged: the stationarity of  $j$  and  $\omega$ , the gradient value  $\nabla j$  in particular. In practice, the present minimization processes have been stopped when entering in the “over-fitting zone” i.e. when the model misfits become smaller than the measurement uncertainties. (Here the virtual surface elevation  $H^{obs}$  are supposed to be accurate at  $+/- 10$  cm). This convergence criteria has always been reached in approximatively 30 iterations, see Fig. 8.

490 *Orders of magnitude and accuracy.* The sough quantity  $\eta$  presents few orders of magnitude (hence this log change of variables) but also with extremely stiff local variations. This features make the inverse problem particularly challenging in terms of numerics.

Then the obtained numerical accuracy (on the optimal diffusivity  $\eta^*$ ) is not as accurate as it can be expected in a standard linear-quadratic case. Typically, for a standard linear-quadratic VDA problem (with more gentle control variable variations) a few % error can be easily reached; on the contrary, in presence of the large and stiff variations of the optimal control variable, a dozen of % error only is reached. For more details, we refer to the forthcoming numerical results in next sections.

## 4 The multi-regime test case and first guess derivations

500 In this section, the academic multi-regime test case aiming at assessing the inversion method(s) presented in the previous section is described. The considered multi-regime flows include many features of the real world flows in terms of fluid mechanics (i.e. independently of the measurement difficulties and uncertainties). Following [13][26], the bed topography is defined consistently with the low-band filter feature of these shallow flows; in particular it respects the minimal wave lengths measurable from the surface.

505 First a flow description is proposed and the two measurement scenarios are defined: depth measurements are available downstream the flow (it is the case 1) or laterally, approximatively parallel to a flow line and within a very slow flow area only (it is the case 2). Both cases define difficult inverse problems which have not been solved up to now in the literature.

The sub-regime areas are a-priori defined from the surface velocity thresholds (and verified to be correct a-posteriori). Given the surface observations (elevation and velocities), given the depth measurements at few points (e.g. a flight track over an ice-shed in Antarctica or Greenland), an a-priori slip ratio law  $R_s^{(0)}$  is derived. This a-priori law turns out to be crucial in all the remaining inference process. From  $R_s^{(0)}$  and using the depth estimations derived in the previous section, first guesses of depth are calculated. The resulting depth first guess  $h^{(0)}$  is already an excellent estimation of the true depth. The extremely stiff variations, moreover of few orders of magnitude, of the sough quantity  $\eta$  is highlighted; this feature makes the numerical inversion particularly 515 challenging.

The next steps of the (depth, friction) inferences (including VDA processes) are done in the next sections for different scenarios (Case 1 and Case 2, with exact or perturbed measurements).

### 4.1 Flow description

520 The geometrical domain  $\Omega$  is a square of length  $L=100$  km. The surface elevation  $H$ , the slopes  $\mathcal{S}$ , and the bed elevation  $b$  are presented in Fig. 3. The flow presents the whole range of slip ratio  $R_s$ : from 0.02 to 0.98, see Fig. 2; hence this flow contains the three sub-regimes.

525 The bed presents sinusoidal variations which are consistent with the mesh size ( $\approx 10$  points minimum per wave length) and consistent with the depth ( $\approx 5$  depth values minimum per wave length). For more details on the shallow ice flow filtering features, the reader can refer to the detailed and complementary analysis presented in [13, 26].

530 The test case definition is a crucial point to assess in a reliable way the inference method. It has to represent a real like flow (hence multi-regime) and it has to be consistent with the shallow ice flow - xSIA model filtering features. The flow is assumed to be isothermal with  $q = 3$  and  $A = 3.10^{-24}$  (this value corresponds to ices at  $\approx -5^\circ C$ ); also:  $\rho = 934$  and  $g = 9.81$ .

The bed elevation is defined by:  $b(x, y) = 150 \sin(\frac{6\pi}{L}x) \sin(\frac{6\pi}{L}y) + 400 e^{-\frac{(y-\frac{3}{2}L)^2}{2 \times 9e07}} + 200 e^{-\frac{(y-L/2)^2}{2 \times 9e07}}$ .

The friction coefficient is defined by:  $C(x, y) = \frac{A1000}{q+2} \frac{1}{50} \left[ 1 + 50^2 \exp(-\frac{(y-L/2)^2}{2 \times 9e07}) + 50 \exp(-\frac{(y-L/2)^4}{(2 \times 9e07)^2}) \right]$ .

The definitions of  $b$  and  $C$  above generate a canyon draining a faster ice stream, see Fig. 2.

535 The surface elevation  $H$  is obtained by solving the xSIA equation (14)(15) with Dirichlet boundary conditions. The latter read:  $H(x, y) = 1000 - 5 \cdot 10^{-3}x$  for all  $x \in \partial\Omega$ . Hence the lateral boundary surfaces present a longitudinal mean slope equal to 5‰.

The computational finite element mesh is a structured triangular mesh 140x140 with refinements in the sharpest bed variation areas, in particular in the vicinity of the left boundary of the canyon. The resulting

Sub-regime	Velocity norm $ \mathbf{u}_H $ (m/y)	Corresponding slip ratio $R_s$
sr1: fully sheared	$ \mathbf{u}_H  < 1$	$R_s \gtrsim 0.8$
sr2: intermediate	$1 \leq  \mathbf{u}_H  \leq 10$	$0.1 \lesssim R_s \lesssim 0.8$
sr3: full sliding	$ \mathbf{u}_H  > 10$	$R_s \lesssim 0.1$

Table 1: Sub-regime area definitions (from the surface velocity norm).

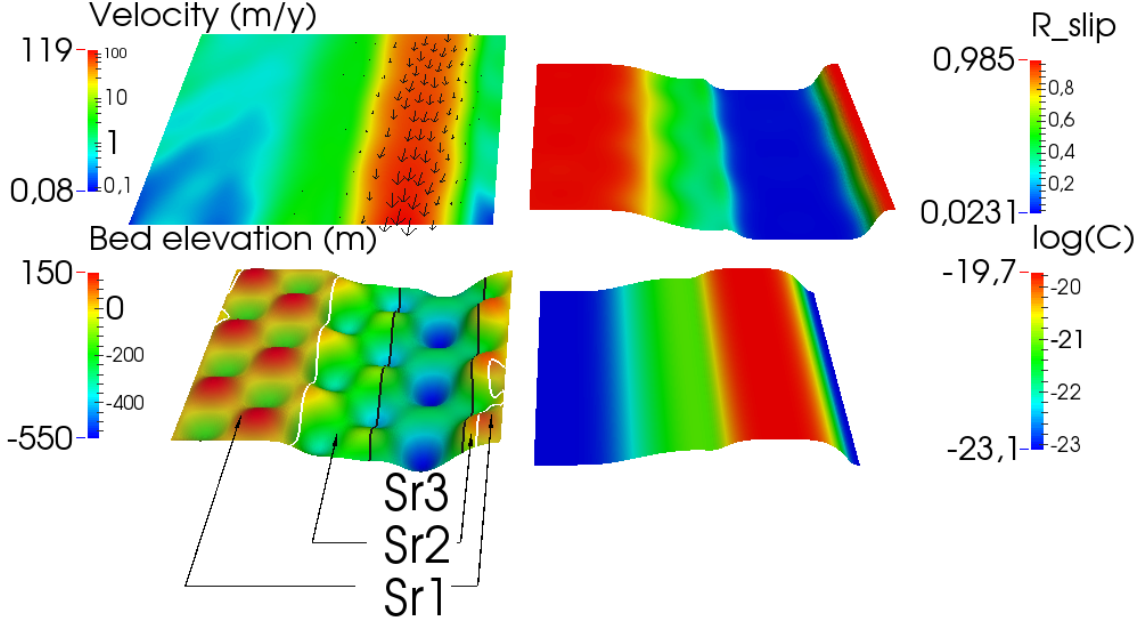


Figure 2: The multi-regime test case. (Up) Left: surface velocity  $\mathbf{u}_H$  (in m/y). Right: slip ratio  $R_s$ . (Down) Left: bed elevation  $b$ . (in m) Right: friction coefficient  $C$  (in log scale). White lines on the bed elevation denote the sub-regime boundaries defined by Table 1.

surface elevation  $H$  and slope values  $\mathcal{S}$  are plotted in Fig. 3. The surface slopes are defined for each mesh triangle; they range from 0.3 % to 0.8%.

It can be noticed that the bed bumps have a clear effect on the top surface slopes. On the contrary, the canyon location cannot be visually detected neither from the surface elevation nor from the surface slopes, see Fig. 3.

Let us point that the sinusoidal bed variations respect the minimal wavelengths not fully filtered by the (shallow) flow, see the complimentary studies [13] and [26]. Also the minimal grid points per wave length is respected.

Let us point out that the regime transitions are mainly due to the friction coefficient variations, see Fig. 2, and these variations are extremely stiff: few orders of magnitudes within a narrow space region (hence almost discontinuities with 1 or 2 order of magnitude gaps). Then a numerical inference of this parameter is obviously very difficult. Nevertheless the forthcoming numerical results demonstrate that the present approach makes possible an accurate depth inference despite this extremely stiff variations of  $C$ .

**Sub-regime zone definitions** From the surface velocity norm  $|\mathbf{u}_H|$ , three sub-regimes areas are a-priori defined. These three sub-regimes areas correspond approximatively to the slip ratio  $R_s$  indicated in Table 1.

The resulting sub-regimes boundaries are plotted in white and black on the bed elevation maps, see e.g. Fig. 2.

The white lines denote the sub-regime 1 boundaries, the black lines denote the sub-regime 3 boundaries; hence the sub-regime 2 area is defined by the white and black lines.

**On the large variations and few orders of magnitude of  $\eta$**  The surface velocity presents 3 orders of magnitude (from 0.1 to 100m/y). In the present test case (which is representative of many real ice-sheds), this leads to a friction coefficient  $C$  presenting 4 orders of magnitude, see Fig. 2. Then the observational quantity  $\mathcal{Q}_H$  defined by (16) presents 3-4 orders of magnitude too, see Fig. 4.

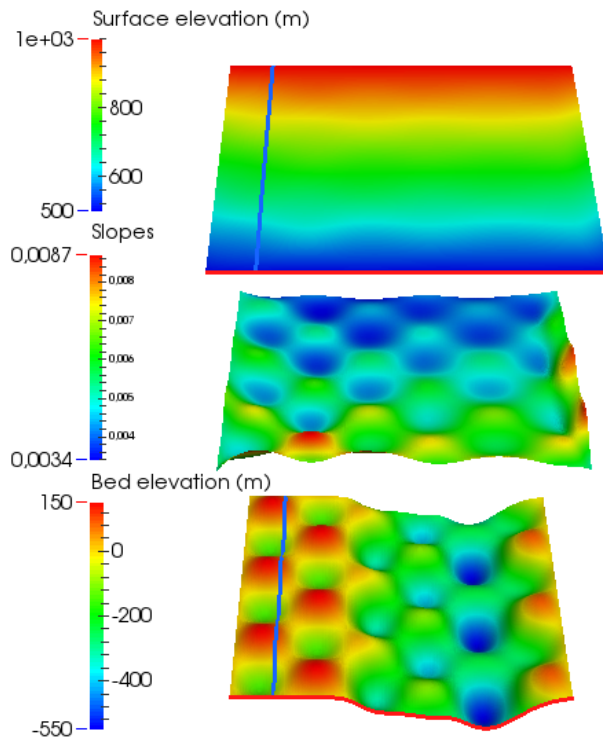


Figure 3: The multi-regime test case. Up: surface elevation  $H$  (in m). Middle: slope values  $\mathcal{S}$ . Down: bed elevation  $b$  (in m). The lateral blue line and the downstream red line (figures up and down) denote the depth measurement locations (e.g. flight tracks)

The effective diffusivity  $\eta$  defined by (15) is plotted in Fig. 4. This quantity  $\eta$  presents patterns very similar to  $\mathcal{Q}_H$  ones, with 4 orders of magnitude too.

The effective diffusivity  $\eta$  will be computed by a VDA process. Its large and locally stiff variations makes its numerical inference very difficult, despite the optimal control problem is mathematically well-posed, and even linear-quadratic with respect to the  $\eta$  variable. The forthcoming numerical results confirm the stiffness of this numerical inverse problem.

Let us notice that these large variations are due to the depth variations and not to the regime (or equivalently slip ratio) variations. Indeed, in the sub-regime 1 case, if setting  $C = 0$ ,  $R_{slip} = 1$ , then:  $\eta_{sr1} = \frac{2A}{(q+2)}h^{q+2}$ . Hence  $\eta$  varies with few orders of magnitude since  $\eta \sim h^{q+2}$ .

Also, in the case of sub-regimes 2 and 3,  $\eta = \eta_{sr1} + Ch^{q+1}$ . Typically for  $R_s = 0.5$ ,  $(q+1)C = 2Ah$  and:  $\eta = [\frac{(2q+3)}{(q+1)(q+2)}]2Ah^{q+2} = \frac{(2q+3)}{(q+1)}\eta_{sr1}$ . In the case  $q = 3$ , it gives:  $\eta = \frac{9}{4}\eta_{sr1}$ . Therefore the large variations of  $\eta$  are not due to the regime variations but to the depth variations.

**Measurements: 2 scenarios** In the following the depth  $h$  is inferred following the method described previously, next the friction coefficient  $C$  is inferred. Two scenarios depending on the measurement locations will be considered:

- Case #1: the depth is measured downstream the flow, see the red line in Fig. 3.
- Case #2: the depth is measured laterally only, following the blue line in Fig. 3.

Both cases are hard inverse problems (and unsolved up to now) for few reasons.

In Case #1, the measurement is available downstream and not upstream, hence any method based on an hyperbolic equation (even regularized by artificial diffusion for example), e.g. the depth mass equation, can infer a reliable depth since the given information is downstream and not upstream of the characteristics. The present model is elliptic hence the inversion robustness is quite the same independently on the measurement location(s).

A-priori, Case #2 is a even harder inverse problem since the measurements “miss” the canyon hence “miss” the large bed variations. Then a a-priori relationship between the surface velocity and the bed variations cannot be directly deduced from the measurements.

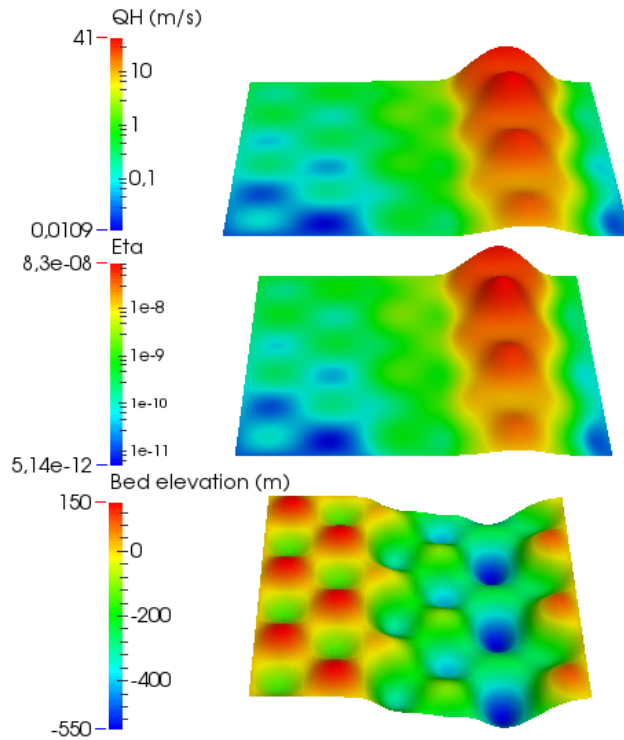


Figure 4: The multi-regime test case. Down: bed elevation  $b$  (in m); Middle: effective diffusivity  $\eta$ (in log scale); Up: observed quantity  $\mathcal{Q}_H$  (in log scale).

One of the key point of the inference method(s) is the quality of the first guess; the latter being deduced from the surface observations, the depth measurements and some expertise. To define a first guess of depth  $h$ , first a a-priori slip ratio law/map  $R_s$  is constructed.

## 4.2 From the measurements to a-priori slip ratio maps

As already mentioned, the depth measurements provide  $(H, h)$  along the lines/tracks indicated in Fig. 3. Combined with the surface measurements  $(H, \mathbf{u}_H)$ , these local depth measurements provide a *local slip ratio law* since  $R_s$  can be written as a function of  $h$  and  $\mathcal{Q}_H$ , see (17). Recall  $q$  and  $\underline{A}$  are given.

The slip ratio law  $R_s$  vs the surface velocity  $\mathbf{u}_H$  is plotted in Fig. 14; the slip ratio law  $R_s$  vs the (complete) observational term  $\mathcal{Q}_H$  is plotted in Fig. 6.

The measurements are plotted for the two scenarios: the downstream measurements case (Case 1) and the lateral measurements case (Case 2). In the case 2, the measured slip ratio range is extremely small hence making the inverse problem particularly difficult. Then two extra empirical values are added to the measurement values:  $(\mathbf{u}_H = 1\text{m/y}, R_s = 0.5)$  and  $(\mathbf{u}_H = 20\text{m/y}, 0.03)$ , see Fig.5 (Right). These two extra values are the two isolated points indicated in green in Fig. 5 (Right) and Fig. 6 (Right).

The complete relation  $R_s(\mathcal{Q}_H, h)$  for all points of the computational domain is plotted in all figures (blue crosses).

The two extra empirical values (potential based on expertise) make fit quite well the slip ratio law throughout the flow, see Fig. 5 (Right).

Next, given the measured slip ratio graph(s) (the blue points), a least-square approximation gives an *a-priori slip ratio law*  $R_s^{(0)}$ . This a priori slip ratio law can be deduced from the surface velocity  $\mathbf{u}_H$  only, Fig. 5, or from the complete surface observational term  $\mathcal{Q}_H$ , Fig. 6.

It turns out that the variation range of  $\mathcal{Q}_H$  is much larger than those of  $\mathbf{u}_H$  only. Then it seems more adequate to define the a-priori slip ratio law  $R_s^{(0)}$  from the slip ratio law in function of  $\mathbf{u}_H$ , and not in function of  $\mathcal{Q}_H$ .

A comparison between the obtained two a-priori slip ratio laws is made in Fig. 7. As expected, the velocity-derived law is closer to the sough pattern (i.e. the true slip ratio map). It can noticed in Fig. 7 that the  $\mathcal{Q}_H$ -derived law makes appear the bed bumps since the presence of  $\mathcal{S}^{-q}$  in the definition of  $\mathcal{Q}_H$ .

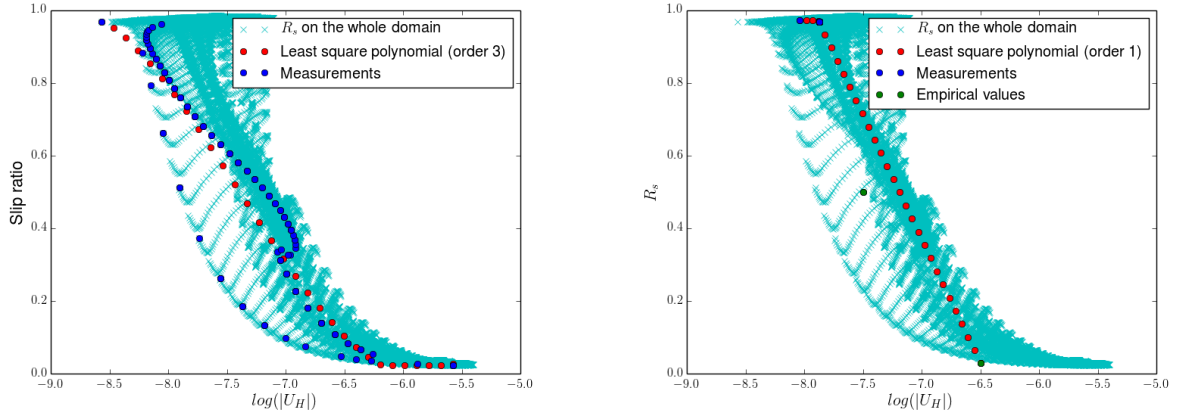


Figure 5: Slip ratio vs  $|\mathbf{u}_H|$  (in log scale) for test case 1 (downstream measurements) (Left) and test case 2 (lateral measurements) (Right). The blue dots are the measurements. The cyan crosses are the values throughout the domain (they are not measured). The red dots are the resulting a-priori slip ratio law, obtained by least-squares.

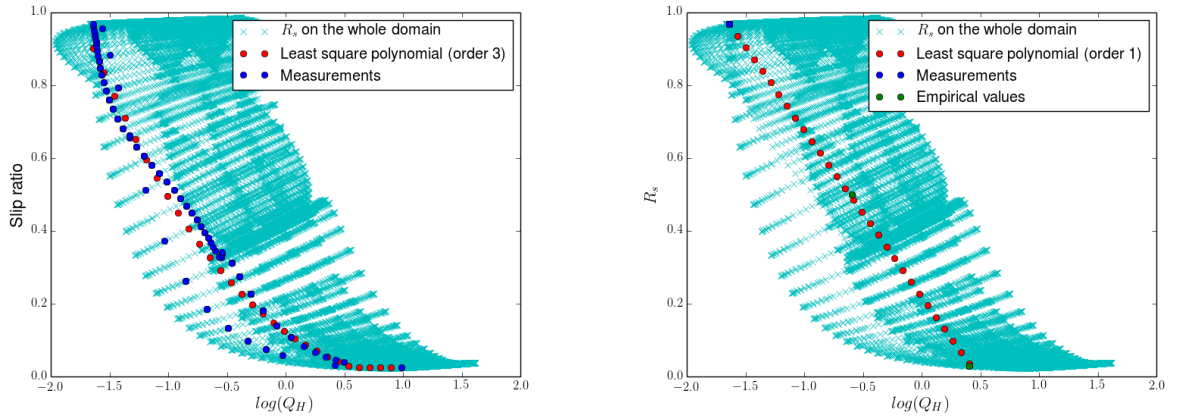


Figure 6: Slip ratio vs  $Q_H$  (in log scale) for test case 1 (downstream measurements) (Left) and test case 2 (lateral measurements) (Right). The blue dots are the measurements. The cyan crosses are the values throughout the domain (they are not measured). The red dots are the resulting a-priori slip ratio law, obtained by least-square.

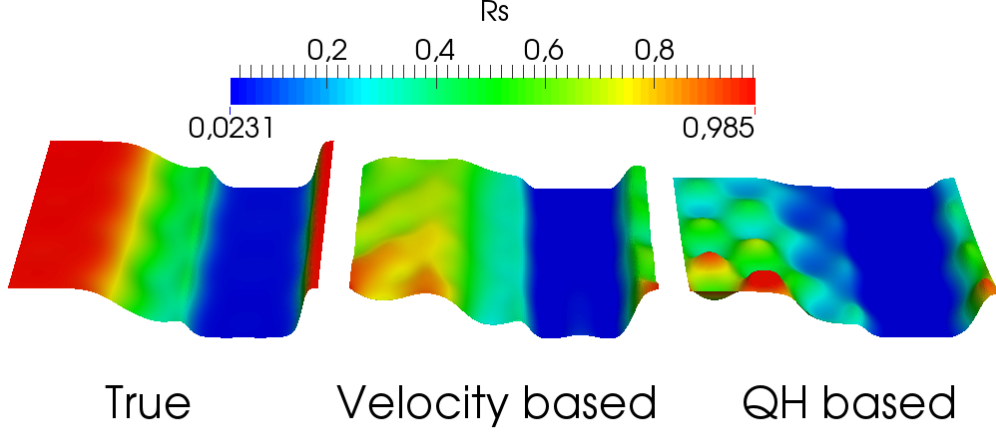


Figure 7: Slip ratio maps. (Left) True values. (Middle) A-priori law derived from  $\mathbf{u}_H$  only. (Right) A-priori law derived from  $\mathcal{Q}_H$ .

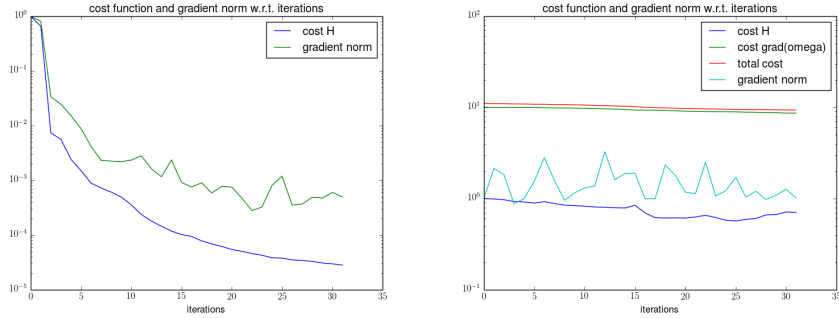


Figure 8: Cost function and gradient norm vs minimization iterations (L-BFGS algorithm) for test case1 with exact measurements.

(Left): VDA#1: misfit term only. (Right) VDA#2: cost function = regularization term + misfit term

### 4.3 First guesses

The VDA process aims at inferring the effective diffusivity  $\eta$ , next the depth  $h$  can be deduced, next the friction coefficient  $C$ . This VDA process requires a first guess  $\eta^{(0)}$ . To define this first guess  $\eta^{(0)}$ , a depth first guess  $h^{(0)}$  is first defined as a straightforward by-product of the a-priori slip ratio map  $R_s^{(0)}$ . Recall that given the observational surface term  $\mathcal{Q}_H$ , given the slip ratio law  $R_s$ , the depth expression reads:

$$h(\mathcal{Q}_H, R_s) = \left[ \frac{(q+1)}{2\rho A} \mathcal{Q}_H R_s \right]^{\frac{1}{(q+1)}} \quad (32)$$

This depth estimation is valid in all sub-regime cases. Then the first guess  $h^{(0)}$  is defined as follows:  $h^{(0)} = h(\mathcal{Q}_H, R_s^{(0)})$  where  $R_s^{(0)}$  is the a-priori slip ratio map defined previously. Next, given this first guess  $h^{(0)}$ , a first guess  $\eta^{(0)}$  can be explicitly obtained from the polynomial expression (22).

Let us point out that the accuracy of  $h^{(0)}$  depends on the accuracy  $R_s^{(0)}$ ; also the expression (32) with  $R_s = 1$  gives (19). In the present test cases, it turns out that for high values of  $R_s$  (sub-regime 1 case),  $h$  directly defined from (19) is more accurate than if evaluating (32). This is due to the quite low accuracy of  $R_s^{(0)}$  for high values, see e.g. Fig. 16.

For comparison, the first guess  $h^{(0)}$  defined by (32) everywhere is plotted in Fig. 9 (exact data case) while those defined by (19) in the sub-regime 1 and (32) elsewhere is plotted in Fig. 11: compare the two first guesses in the sub-regime 1 area.

Finally, observe that the present method consisting to derive a first guess  $\eta^{(0)}$  does not require an *explicit* friction coefficient first guess. This is an important feature and a strength of the present inversion method since the uncertainties on the (empirical) friction coefficient  $C$  are large; hence it would be a real issue to define directly a reliable first guess on this quantity.

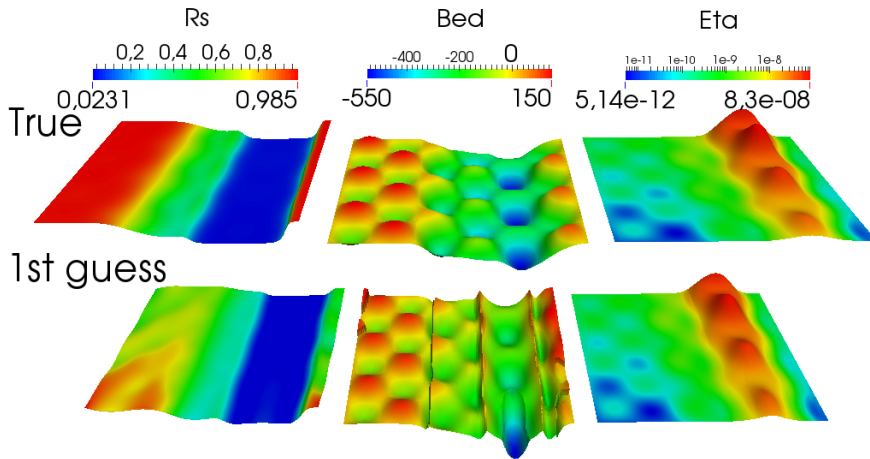


Figure 9: Test case 1 with exact measurements. (Top) True values. (Down) 1st guess values. From left to right : slip ratio  $R_s$ , bed elevation  $b$  (in m) inferred from (32), effective diffusivity  $\eta$ (log scale).

## 5 Case 1: downstream measurements

In this section, the numerical results obtained in the case of downstream measurements (red tracks in Fig. 3) are presented and analysed. First, the inference process is performed from the exact data; Second, it is performed from perturbed data (the exact surface measurement  $Q_H$  plus a random noise).

The complete inverse method is as follows: first guesses are evaluated from the various analytical formula as described in the previous section; next the VDA process described previously is performed to estimate the effective diffusivity  $\eta$ ; next the depth  $h$  (or equivalently the bed elevation  $b$ ) is obtained in the whole domain. Finally the corresponding friction parameter  $C$  can be explicitly deduced. Recall that in the sub-regime 1 areas, the analytical formula (19) is sufficient to infer the depth hence not requiring the VDA process.

### 5.1 Exact measurements

Given the downstream depth measurements, see Fig. 3, given the exact surface data  $(H, \mathcal{S})$ , the VDA process (28)-(30) is performed in two steps:

- VDA#1: the cost function contains the misfit term only, i.e.  $\alpha_\eta = 0$  in (29).
- VDA#2: the regularization term is added to the cost function, see (29). The goal of this second VDA process is to obtain a reasonably smooth solution while fitting the data.

After each VDA process, the two depth estimations (19) and (25) are explicitly obtained while the sub-regime 2 depth estimation  $h_{sr2}$  is obtained by solving numerically the polynomial (22). The polynomial roots are classically obtained by computing the eigenvalues of the corresponding companion matrix (by employing the Python procedure `numpy.roots`). The selected root value is those belonging to the interval  $[h_{sr3}, h_{sr1}]$ . If imaginary, the real part only is considered.

#### 5.1.1 VDA#1: fitting data only

The VDA problem (28)-(30) is numerically solved with  $\alpha_\eta = 0$ . As detailed previously, an a-priori slip ratio map  $R_s^{(0)}$  is defined, next a depth first guess  $h^{(0)}$ , next the first guess  $\eta^{(0)}$ . These first guesses are presented in Fig. 16. It can be noticed that the resulting depth first guesses  $h_{sr\Box}^{(0)}$  are already an excellent estimation of the true depth. From a “single” downstream measurement plus the observed surface term  $Q_H$ , the inferred bed without performing the VDA process is already accurate, see Fig. 16.

Next VDA#1 process is performed. The cost function and gradient vs minimization iterations are plotted in Fig. 8. From the obtained optimal value  $\eta^*$ , the three depth estimations are computed; they are plotted in Fig. 10. The three estimates give quite accurate results in their respective domain of validity. Typically  $h_{sr1}$  is accurate to within 5% (and less) in the sub-regime 1 area;  $h_{sr2}$  (resp.  $h_{sr3}$ ) is accurate to within 10% in the inner part of the sub-regime 2 area (resp. sub-regime 3 area) and accurate to within 20% at the area boundaries.

The large variations and stiff variations of  $\eta$  between the different sub-regime areas makes the numerical inverse problem difficult. The numerical inferred value  $\eta$  is relatively less accurate, hence the less accurate depth estimation in these areas. Concretely, it gives the local “peaks” of errors ( $\approx 25\%$  error) plotted in Fig. 10.

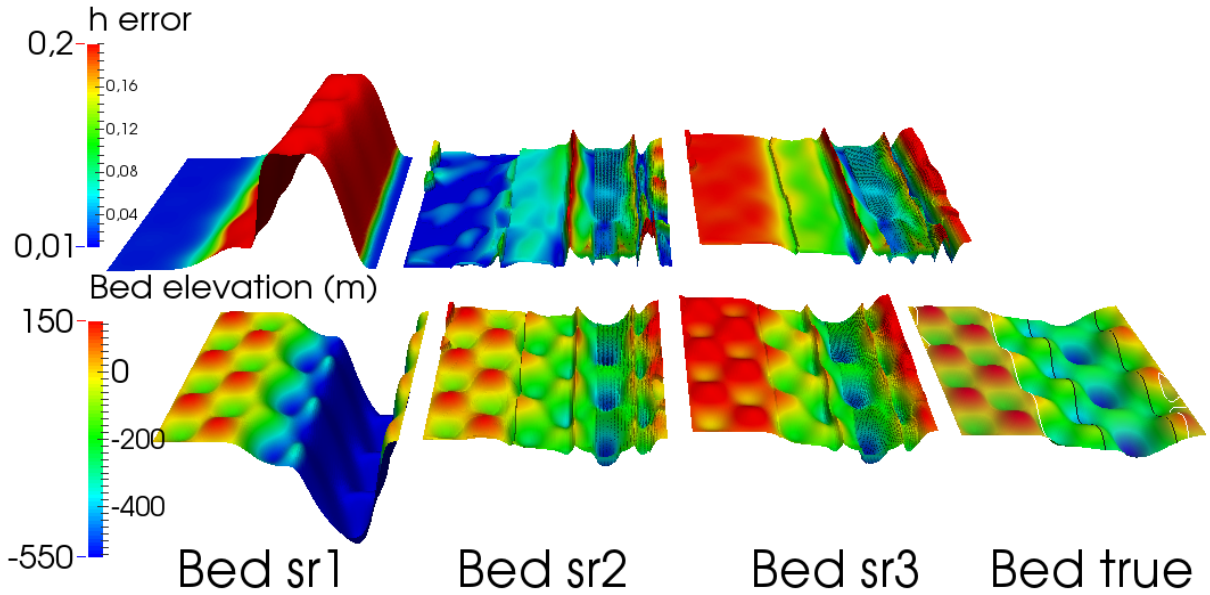


Figure 10: Test case 1 with exact measurements; depth obtained after VDA#1. (Down) From left to right :  $h_{sr1}$ ,  $h_{sr2}$ ,  $h_{sr3}$  and true value (with the lines indicating the sub-regimes areas defined by Table 1). (Top) From left to right : corresponding relative errors (for each  $h_{sr\Box}$ ).

Error	First guess	After VDA #1	After VDA #2
$\frac{\ h-h_{true}\ _2}{\ h_{true}\ _2}$	0.099	0.084	0.076
$\frac{\ h-h_{true}\ _\infty}{\ h_{true}\ _\infty}$	0.443	0.443	0.443
$\ H - H_{obs}\ _\infty$	14.08	0.15	0.19
$\frac{1}{n} \ H - H_{obs}\ _2$	0.0446	0.0002	0.0002

Table 2: Test case #1 with exact measurements: global errors (throughout the domain). (The errors on  $H$  are obtained by running the direct model).

675 In other respect, let us recall that by construction the sub-regime2 depth derivation, see (22), is valid everywhere; it includes the three sub-regime cases. Hence the sub-regime 2 estimation  $h_{sr2}$  is valid throughout the computational domain. However, it is not necessarily the most accurate estimation, see Fig. 10, since the respective simplifications made to obtain  $h_{sr1}$  and  $h_{sr3}$  circumvent the potential errors made on the a-priori slip ratio law  $R_s^{(0)}$ . Therefore these simplified estimations give more accurate values; this is particularly true in  
680 the sub-regime 1 case, see Fig. 10.

Following the a-priori definitions of the sub-regime areas, see Table 1, the combination of the 3 estimations  $h_{sr\Box}$  gives the global bed inference plotted in Fig. 11. At the sub-regime limits, corresponding to the large and stiff variations of  $\eta$ , the relative error on  $b$  equals approximately 20% (corresponding to the “linear peaks” plotted in Fig. 11). Out of these stiff regime transition areas, the relative error is smaller than 10%.

685

### The resulting friction field

Let us recall that in the present inverse method, the friction coefficient is a simple by-product of the depth inference. In other words, the present method makes possible to separate the two crucial basal fields: the bed and the friction. In other words, the present method makes possible to separate the two crucial basal fields: the bed and the friction. Given a depth estimation, it is straightforward to compute the friction coefficient either from (26) or from (27). Numerically, both give extremely close values. The resulting friction coefficient is plotted in Fig.12. The blue parts correspond to the sub-regime 1 areas. In these areas, a threshold has been applied (to a very low value); this threshold being defined such that  $C \ll Ah$ , see (15). Then the relative error in the sub-regime 1 is meaningless. In the sub-regime 2 area (resp. sub-regime 3), the error is globally between 10% and 60%, excepted where the depth error is higher. Then at the sub-regime limits, the error on the friction field can reach 100%.

As expected, the estimated friction is accurate where the estimated depth is accurate. On the contrary where the estimated depth is less accurate, the estimated friction coefficient can't be accurate since it is implicitly set such that it makes fit the model outputs with the observations. Somehow this friction coefficient absorbs all errors (including the modeling errors which are null in the present study).

700

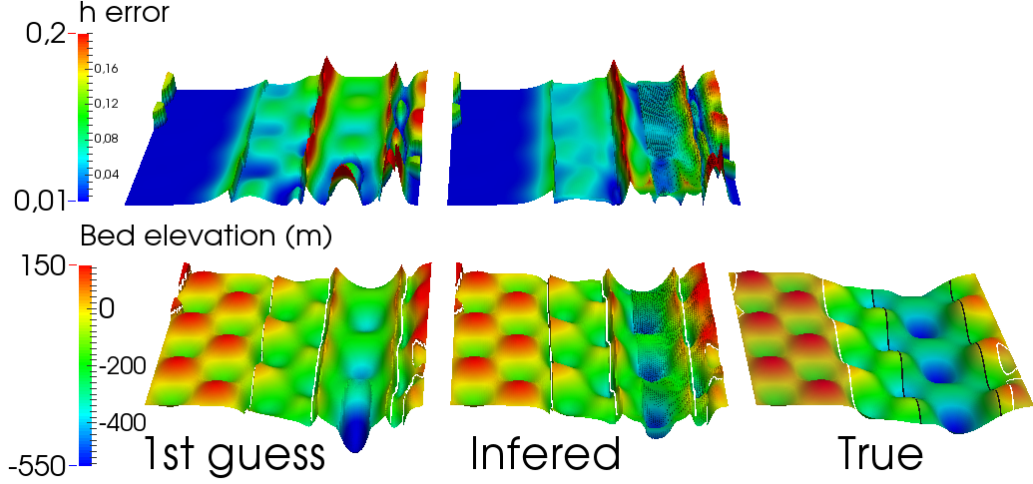


Figure 11: Test case 1: Bed elevation after VDA#1, with exact measurements. (Down) From left to right: 1st guess, inferred value after VDA#1, true value (with the lines indicating the sub-regimes areas defined by Table 1). (Top) Corresponding relative errors. The white lines denotes the different regime zones.

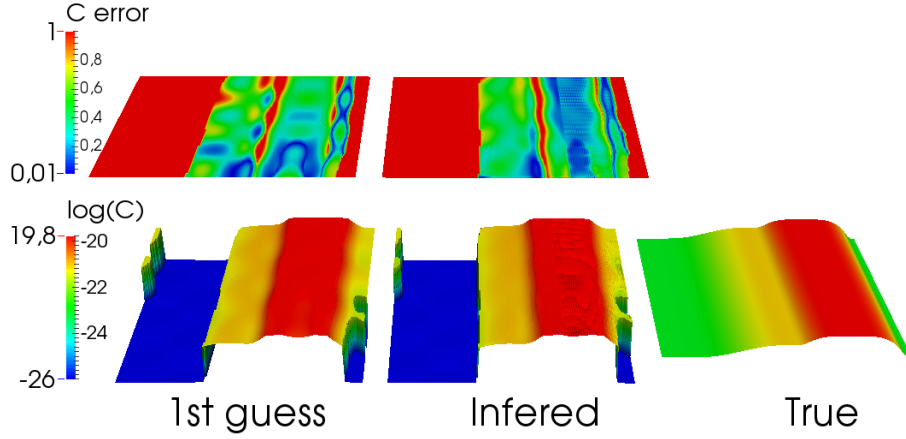


Figure 12: Test case 1: friction coefficient  $C$  after VDA#1, with exact measurements. (Down) From left to right: 1st guess, inferred value after VDA#1, true value. (Top) Corresponding relative errors.

Finally let us recall that the regime transition are mainly due to the friction coefficient variations, see Fig. 2, and these variations are extremely stiff: few orders of magnitudes within a narrow space region. Then a numerical inference of this parameter is obviously very difficult. Nevertheless the numerical results demonstrate that the present approach makes possible an accurate depth inference despite this extremely stiff variations of  $C$  (variations being almost discontinuities with few order of magnitude gaps).

### 5.1.2 VDA#2: smoothing process

The first VDA process (VDA#1) was deliberately taking into account the observational term only. The goal was to analyse the inference capabilities of the present mix analytical-VDA method. From this VDA#1 optimal solution  $(\eta^{\#1}, h^{\#1})$ , a second VDA process is performed. The goal is to smooth the solution while keep fitting the data.

The control variable is still  $\omega = \ln(\eta)$ . The cost function  $j(\omega)$  is defined by:  $j(\omega) = \alpha_H j_H(\omega) + \alpha_\omega j_\omega(\omega)$ , with

$$j_H(\omega) = \frac{1}{2} \int_{\Omega} |H^\omega - H^{obs}|^2 dx \text{ and } j_\omega(\omega) = \frac{1}{2} \int_{\Omega} |\nabla \omega|^4 dx, \quad (33)$$

with  $\alpha_H = 1$  and  $\alpha_\omega = 20$ . The regularizing weight parameter  $\alpha$  is set following an empirical L-curve criteria, see e.g. [14]. The cost function and gradient norm vs minimization iterations is plotted in Fig. 8 right.

The minimization process makes decrease both the regularization term and the misfit term. The resulting fields

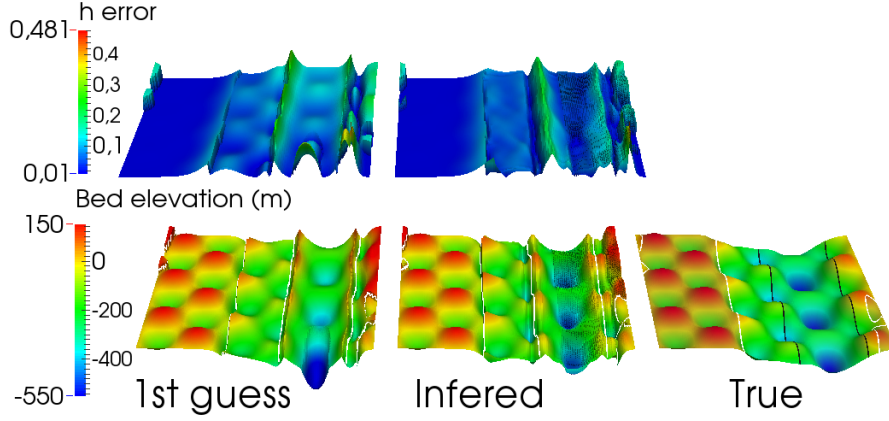


Figure 13: Test case 1: bed elevation after VDA#2, with exact measurements. (Down) From left to right: 1st guess, inferred value after VDA#2, true value. (Top) Corresponding relative errors. The white lines denotes the sub-regime area boundaries defined from Table 1.

are plotted in Fig. 13 and Tab. 2. This second VDA process makes decrease the error mainly in the stiff variations of  $\eta$  (the “error peaks” located at the sub-regimes boundaries), making decrease approximatively the error peaks from 20% to 15%. Furthermore, VDA#2 slightly makes improve the accuracy everywhere else by a few % (compare Fig. 13 and Fig. 11).

720

## 5.2 Uncertain surface measurements: (quasi-)explicit sensitivities

The surface measurements are the surface elevation  $H$  (potentially acquired by altimetry) and the surface velocity  $\mathbf{u}_H$  (potentially acquired by InSAR techniques). From these measurements, the slopes  $\mathcal{S}$  and the observational term  $\mathcal{Q}_H$  defined by (16) can be estimated. The uncertainty sources are numerous and the resulting accuracy on  $\mathcal{Q}_H$  depends on many factors. Typically, the error measurements in  $H$  can be a-priori considered uniform in space; on the contrary the error measurements in  $\mathbf{u}_H$  depends on its amplitudes, hence depending on the sub-regime areas. Finally let us remark that the observational term  $\mathcal{Q}_H$  is linear in  $\mathbf{u}_H$  (hence introducing some noise in  $\mathbf{u}_H$  is equivalent to introduce the same noise in  $\mathcal{Q}_H$ ); this is different with respect to the slopes since  $\mathcal{Q}_H \sim \mathcal{S}^{-q}$ .

725

### 5.2.1 The depth estimations $h_{sr}$ vs observational term perturbations $\delta\mathcal{Q}_H$

730

Let us analyse the sensitivity of the three depth estimations with respect to perturbations on  $\mathcal{Q}_H$ . This analysis is crucial in term of robustness of the inversion method, and sensitivity with respect to the error measurements. Recall that  $\mathcal{Q}_H$  is defined by (16) hence varies linearly in  $\mathbf{u}_H$  and varies in  $\mathcal{S}^{-q}$ .

The error measurements come independently from  $\mathbf{u}_H$  and  $\mathcal{S}$ . Concerning the slope values  $\mathcal{S}$ , an additional issue may be addressed: at what scale the numerical model has to be set up? This slope scale questioning is classical and is difficult to tackle. However the slope scale is a global concept, then the answer (given in terms of length factor) is the same everywhere in the computational domain. From the sensitivity analysis below, an approach to identify the correct slope scale of the xSIA model is suggested in next section.

735

Let us present a sensitivity analysis of the three depth estimations with respect to variations of  $\mathcal{Q}_H$ . We denote by  $h(1 + \delta h)$  the resulting depth of a perturbed observational term  $\mathcal{Q}_H(1 + \delta\mathcal{Q})$ . For each depth estimation, the resulting depth variation  $\delta h$  is plotted vs  $\delta\mathcal{Q}$  in Fig. 14(Left); for a  $[-50, +50]\%$  perturbation range.

740

In the sub-regime 1 case, it follows from (19) that:

$$\delta h_{sr1} = (1 + \delta\mathcal{Q})^{1/q+1} - 1 \quad (34)$$

Therefore the uncertainties on the observational term  $\mathcal{Q}_H$ , or equivalently on the surface velocity  $\mathbf{u}_H$ , is greatly damped, see Fig. 14. A typical example for these fully sheared flows (hence slow flows) is the following: a 30% noise on  $\mathbf{u}_H$  (or equivalently on  $\mathcal{Q}_H$ ) makes  $h_{sr1}^{noise}$  deviate from  $h_{sr1}$  by  $\approx 8\%$  only.

745

In the sub-regime 3 case, it follows from (25) that:

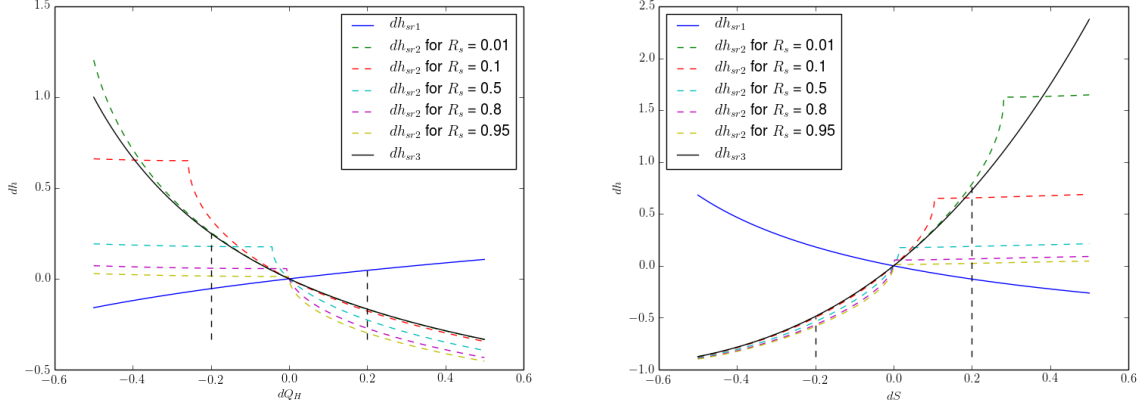


Figure 14: (Left) Explicit depth variations  $(\delta h_{sr1}, \delta h_{sr2}, \delta h_{sr3})$ : (Left) vs  $\delta \mathcal{Q}_H$ ; (Right) vs  $\mathcal{S}$ .  $\delta h_{sr2}$  is obtained by computing the roots of the perturbed polynomial (22). The curves  $\delta h_{sr2}$  are plotted for typical slip ratio values.

$$\delta h_{sr3} = \frac{1}{(1 + \delta \mathcal{Q})} - 1 \quad (35)$$

In the intermediate sub-regime 2 case, the dependency is more complex since the uncertainties propagate into the roots of polynomial (22). As a first step, the estimation (23) shows that if assuming the slip ratio  $R_s$  invariant then the sensitivity of  $h_{sr2}$  with respect to  $\mathcal{Q}_H$  is the same than those in the sub-regime 3 case:  $\delta h = \frac{1}{(1 + \delta \mathcal{Q})} - 1$ . Next to compute the complete sensitivity of  $h_{sr2}$  with respect to  $\mathcal{Q}_H$ , the polynomial (22) has to be numerically solved for each perturbed value of  $\mathcal{Q}_H$ . In Fig. 14 (Left),  $\delta h_{sr2}$  is plotted vs  $\delta \mathcal{Q}$  for the few typical slip ratio values. To plot these curves, the different steps are the following: given a slip ratio  $R_s$ , the corresponding friction coefficient  $C$  is evaluated from (12), next  $\eta$  is evaluated from (15), next  $\mathcal{Q}_H$  is evaluated from (17), and finally the sough root of the polynomial (22) with the perturbed  $\mathcal{Q}_H$  is computed.

For weakly sheared - slipping flows (sub-regimes 2 and 3), hence relatively fast flows, a typical 10% noise on  $\mathbf{u}_H$  makes deviate  $h$  by  $\approx 10 - 20\%$  %, depending on the slip ratio value. Hence realistic uncertainties on the surface velocity  $\mathbf{u}_H$  does not prevent to estimate correctly the depth.

In next section, a  $[-20, +20]\%$  random noise (range indicated by the vertical dashed lines in Fig. 14 (Left)) will be added to  $\mathcal{Q}_H$  before performing the complete inversion process (i.e. including the VDA process).

### 5.2.2 The depth estimations $h_{sr\Box}$ vs slope perturbations $\delta \mathcal{S}$

*The observational term  $\mathcal{Q}_H$  vs slope perturbations  $\delta \mathcal{S}$ .* If perturbing the slope  $\mathcal{S}$  then  $\mathcal{Q}_H$  is perturbed as follows:  $\mathcal{Q}_H(1 + \delta \mathcal{Q}) = \frac{U_H}{S^q(1 + \delta \mathcal{S})^q}$ . Therefore:  $\delta \mathcal{Q} = \frac{1}{(1 + \delta \mathcal{S})^q} - 1$ . Roughly a  $[-10, +10]\%$  (resp.  $[-20, +20]\%$ ) perturbation on  $\mathcal{S}$  leads to a  $[-40, +25]\%$  (resp.  $[-50, +100]\%$ ) perturbation on  $\mathcal{Q}_H$ .

Now, let us compute the depth estimations  $h_{sr\Box}$  vs slope perturbations  $\delta \mathcal{S}$ . As before, we denote by  $h(1 + \delta h)$  the resulting depth of the perturbed observational term  $\mathcal{S}(1 + \delta \mathcal{S})$ .

In the sub-regime 1 case, the direct expression  $\delta h_{sr1}(\delta \mathcal{S})$  is straightforwardly obtained. In the sub-regime 3 case,  $\delta h_{sr3}$  depends on  $\delta \mathcal{S}$  but also on  $\delta \eta$ .

In the sub-regime 2 case, the different steps are the following: given a slip ratio  $R_s$  the corresponding friction coefficient  $C$  is evaluated from (12), next  $\eta$  is evaluated from (15), next  $\mathcal{Q}_H$  is evaluated from (17), and finally the sough root  $h_{sr2}(1 + \delta h_{sr2})$  of the polynomial (22) is computed (root corresponding to the perturbed value of  $\mathcal{S}$  hence  $\mathcal{Q}_H$ ).

In Fig. 14 (Right), the few  $\delta h_{sr\Box}$  values are plotted vs  $\delta \mathcal{S}$ . The difference of behavior between  $\delta h_{sr2}$  and  $\delta h_{sr1}$  (resp.  $\delta h_{sr3}$ ) at high slip ratio value (resp. low value) is remarkable. In particular, for diminishing slopes values,  $\delta h_{sr2}$  and  $\delta h_{sr3}$  behaves similarly. For increasing slopes values,  $\delta h_{sr2}$  is more accurate than  $\delta h_{sr1}$  (for high slip ratio values).

## 5.3 The complete inversion process with an uncertain observational term $\mathcal{Q}_H$

In the previous numerical depth inference, the surface measurements were supposed to be exact. In the present numerical experiment, a 20% random noise is added to  $\mathcal{Q}_H$ . Recall that this perturbation in  $\mathcal{Q}_H$  is equivalent

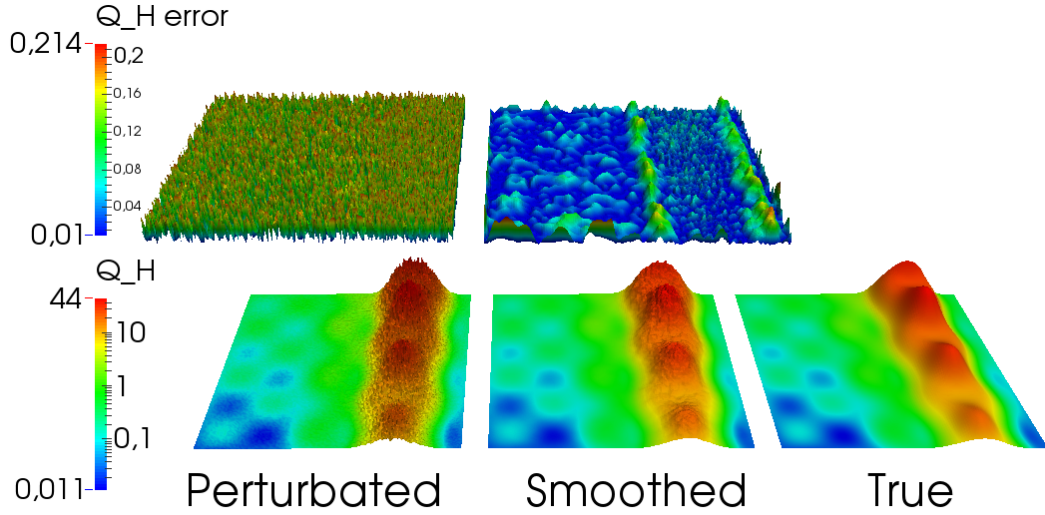


Figure 15: Test case 1: perturbed  $\mathcal{Q}_H$ . (Down) From left to right:  $\mathcal{Q}_H$  with noise, after smoothing process, original “true” field. (Top) The corresponding relative errors.

error	First guess	after VDA #1	after VDA #2
$\frac{\ h-h_{true}\ _2}{\ h_{true}\ _2}$	0.089	0.079	0.075
$\frac{\ h-h_{true}\ _\infty}{\ h_{true}\ _\infty}$	0.533	0.468	0.437
$\ H - H_{obs}\ _\infty$	8.294	0.26	0.27
$\frac{1}{n} \ H - H_{obs}\ _2$	0.0264	0.0004	0.0003

Table 3: Test case #1 with uncertain measurements: global errors (throughout the domain). (The errors on  $H$  are obtained by running the direct model).

to a 20% random perturbation in  $\mathbf{u}_H$ ; or it corresponds approximatively to a 5% random perturbation in  $\mathcal{S}$ , see Fig. 14. Then the consequences of this randomly perturbed  $\mathcal{Q}_H$  to the inferred depth are analyzed.

As a first step, the randomly perturbed  $\mathcal{Q}_H$  is smoothed by minimization the following cost function:

$$g(\mathcal{Q}_H) = \frac{1}{2} \|\mathcal{Q}_H - \mathcal{Q}_H^{obs}\|_{2,\Omega}^2 + \frac{\alpha}{2} \|\nabla \mathcal{Q}_H\|_{2,\Omega}^2 dx \equiv \frac{1}{2} [g_1(\mathcal{Q}_H) + \alpha g_2(\nabla \mathcal{Q}_H)] \quad (36)$$

Again the regularizing weight parameter  $\alpha$  is set following an empirical L-curve criteria. This led to set:  $\alpha = 5.2 \cdot 10^{11}$ . The cost function values ( $g_1(\mathcal{Q}_H), g_2(\nabla \mathcal{Q}_H)$ ) equals:  $(0, 5.2 \cdot 10^{11})$  at the first iteration and  $(1.8 \cdot 10^9, 3.7 \cdot 10^{10})$  at the 32<sup>nd</sup> and last iteration. The corresponding values of  $\mathcal{Q}_H$  are plotted in Fig. 15.

Next the VDA process to compute  $\eta$  is performed. Let us notice that the noise on  $\mathcal{Q}_H$  has a direct impact on the a-priori slip ratio map  $R_s^{(0)}$  then on the first guesses  $\eta^{(0)}$  and  $h^{(0)}$ . The first guesses, computed as described previously, are plotted in Fig. 16. Again, the first guesses  $h_{sr\Box}^{(0)}$  are already excellent estimations of the true values.

Next, the complete VDA process is performed: the VDA#1 process,  $\alpha_\omega = 0$  in (29), next the VDA#2 process with  $\alpha_\omega = 7$ . From the obtained optimal value  $\eta^*$ , the three depth estimations are computed; they are plotted in Fig. 10 and Fig. 18, see also Tab. 3. The three depth estimates  $h_{sr\Box}^{(0)}$  give results roughly as accurate as in the exact measurements case. Indeed  $h_{sr1}$  is accurate to less than 5% in the sub-regime 1 area;  $h_{sr2}$  (resp.  $h_{sr3}$ ) is accurate to 10% (and less) in the inner part of the sub-regime 2 area (resp. sub-regime 3 area) and accurate to 20% at the area boundaries.

Compared to the first depth value, the VDA process improved the solution mainly in the sub-regime 3 area: the error decreases from 10 – 30% before VDA to 5 – 20% after VDA, see Fig. 16 and Fig. 18.

### 800 The resulting friction field

Given the depth  $h$  everywhere, the friction coefficient  $C$  is obtained explicitly by evaluating (26) or (27), both formula giving quite the same values. The resulting friction coefficient is not plotted since its patterns and its accuracy are very similar to the case of exact measurements, see Fig.12.

805 In summary, a 20% random noise on  $\mathcal{Q}_H$  throughout the computational domain (potentially corresponding to a 20% noise on  $\mathbf{u}_H$  or to a 5% noise on  $\mathcal{S}$ ) does not affect the robustness of the present inversion approach nor the accuracy of the inferred depth. Nevertheless this encouraging result has to be tempered since the

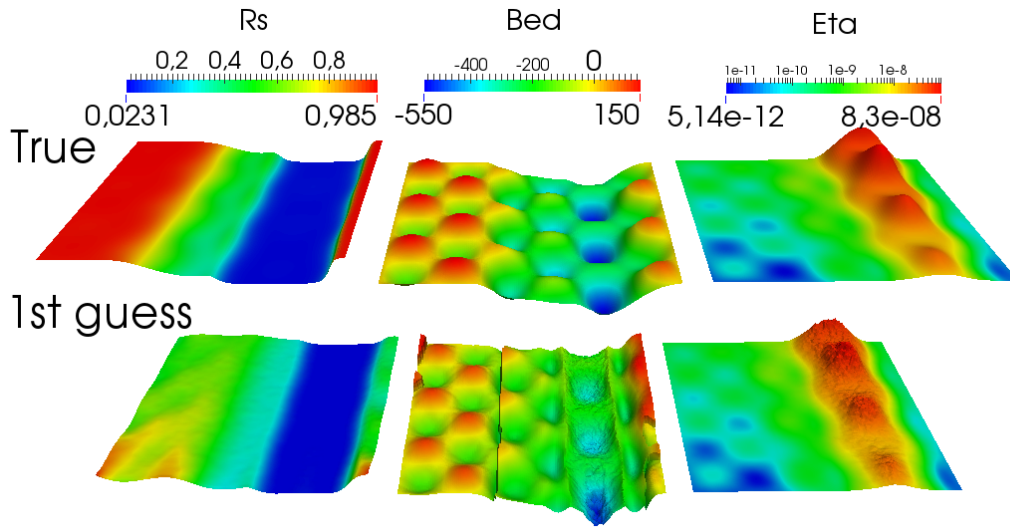


Figure 16: Test case 1 with uncertain measurements (20% random noise on  $Q_H$ ). (Top) True values. (Down) 1st guess values after the smoothing process. From left to right : slip ratio  $R_s$ , bed elevation  $b$  (in m) inferred from (32), effective diffusivity  $\eta$ (log scale).

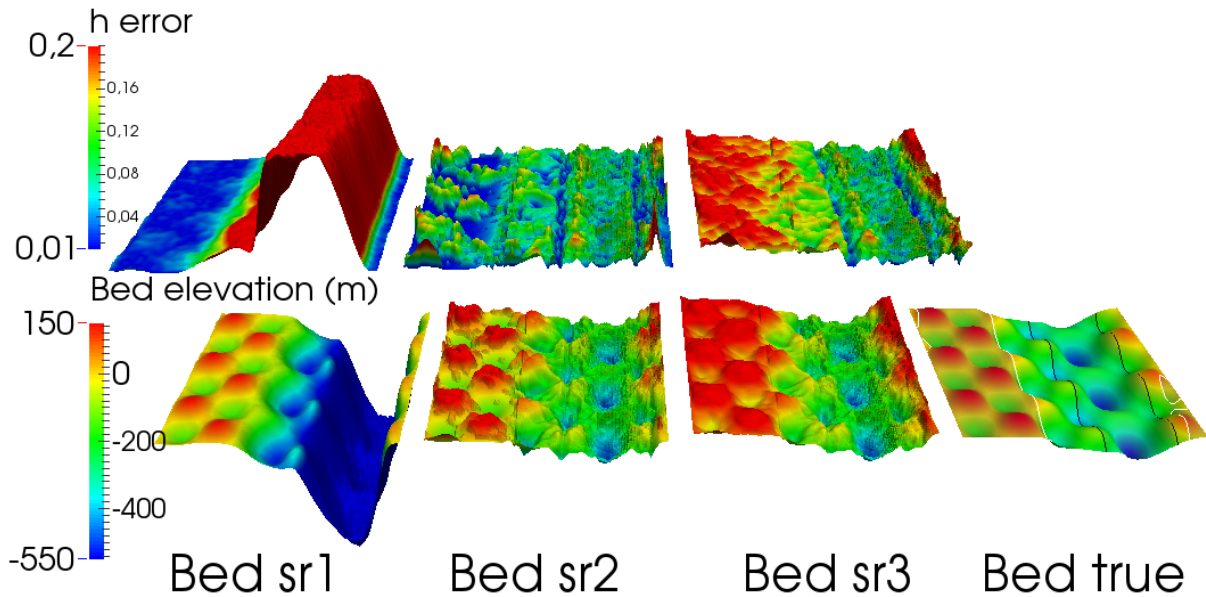


Figure 17: Test case 1 with uncertain measurements (20% random noise on  $Q_H$ ); depth obtained after VDA. (Down) From left to right :  $h_{sr1}, h_{sr2}, h_{sr3}$  and true value (with the lines indicating the sub-regimes areas defined by Table 1). (Top) From left to right : corresponding relative errors (for each  $h_{sr\Box}$ ).

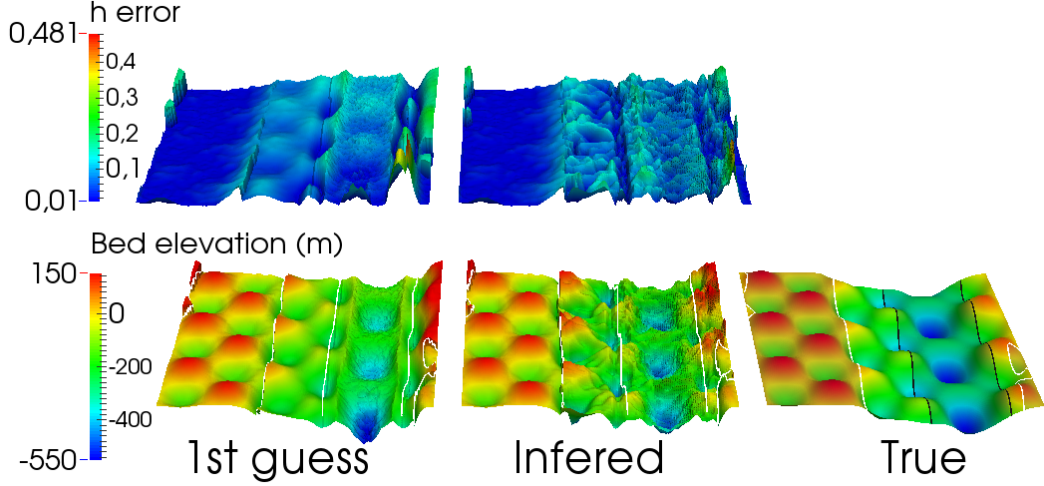


Figure 18: Test case 1 with uncertain measurements (20% random noise on  $Q_H$ ); bed elevation. (Down) From left to right: 1st guess, inferred value after VDA, true value (with the lines indicating the sub-regimes areas defined by Table 1). (Top) Corresponding relative errors. The white lines denotes the different regime zones.

slope term  $\mathcal{S}$  considered in the xSIA equation (14) was considered as exact. Only the observational term  $Q_H$  (appearing throughout the complete inversion process: explicit formulas, first guesses and the VDA process) has been perturbed. The questioning of the slope uncertainty (and/or the slope scale definition) is addressed in a forthcoming section.

## 6 Case 2: lateral measurements

The present numerical experiment is the same as the previous one with exact data but the location of the depth measurements. In the present case, the depth is measured following the lateral line/track indicated in blue in Fig. 3. Consequences are important since the depth measurements are available in a mono-regime area only (fully sheared area) furthermore parallel to a flow line. In particular, these measurements do not include any point in the canyon nor various upstream points. This configuration makes the inverse problem particularly challenging.

### 6.1 First guess

The first step of the inverse method consists to define the a-priori slip ratio map  $R_s^{(0)}$ . In the present configuration, the depth measurements do not include a varying slip ratio, hence extra a-priori have to be made. Then as already mentioned the two a-priori are made:

- a surface velocity  $|\mathbf{u}_H| = 1 \text{ m/y}$  corresponds to slip ratio  $R_s = 0.5$ ,
- a surface velocity  $|\mathbf{u}_H| = 20 \text{ m/y}$  corresponds to slip ratio  $R_s = 0.03$ ,

see the 2 green points in Fig. 5. Given the resulting a-priori slip ratio map  $R_s^{(0)}$ , the first guess  $\eta^{(0)}$  and finally the depth first guess  $h^{(0)}$  are computed as previously described. These first guesses are plotted in Fig. 19, see also Tab. 4. Again, the resulting depth first guess  $h^{(0)}$  is already excellent.

Let us point out that if the a-priori slip ratio is inaccurate, typically by considering the second point equal to  $(2\text{m/y}, 0.03)$  hence leading to a really bad  $R_s^{(0)}$ , see Fig. ??, then the 2-norm relative error in  $h$  is approximatively 20% instead of 7 – 8%, see Tab. 4.

### 6.2 Inferred bed elevation after VDA

Next the VDA process is performed. In the present case, it turns out that the regularization term  $j_\omega$  is not greatly necessary (recall that data are exact), see Tab. 4. Then the presented results are those of VDA#1 only:  $\alpha_\omega = 0$  in (29). The minimization process converges in 30 iterations, reaching the  $\pm 10$  cm uncertainties on the surface elevation.

From the obtained optimal value  $\eta^*$ , the three depth estimations are computed. Next, following the a-priori definitions of the sub-regime areas, Table 1, the combination of the 3 estimations  $h_{sr\Box}$  gives the inferred bed

Errors	First guess	After VDA #1	After VDA #2
$\frac{\ h-h_{true}\ _2}{\ h_{true}\ _2}$	0.084	0.076	0.070
$\frac{\ h-h_{true}\ _\infty}{\ h_{true}\ _\infty}$	0.443	0.443	0.446
$\ H - H_{obs}\ _\infty$	6.89	0.21	0.17
$\frac{1}{n} \ H - H_{obs}\ _2$	0.0236	0.0002	0.0002

Table 4: Test case #2: global errors (throughout the domain). (The errors on  $H$  are obtained by running the direct model).

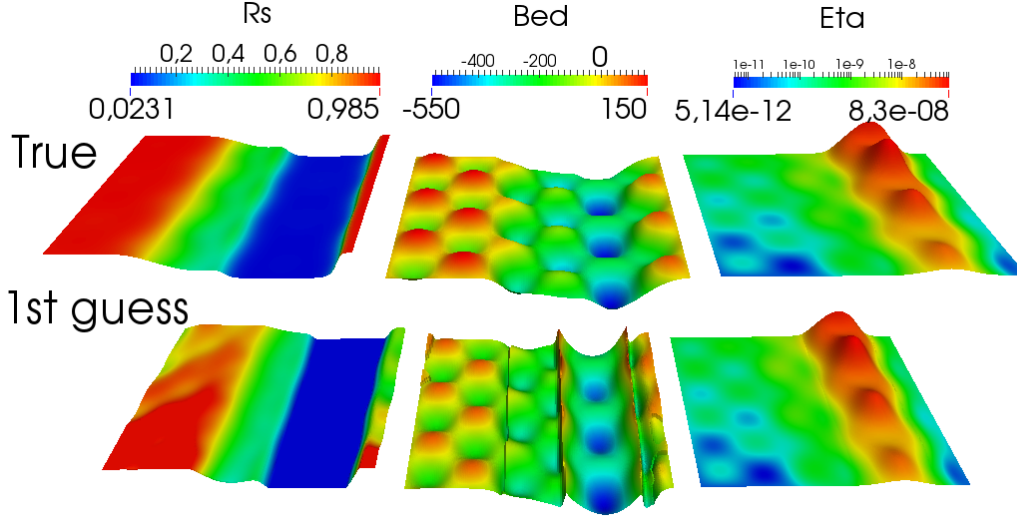


Figure 19: Test case 2 (lateral measurements). (Top) True values (Down) First guess values. From left to right : slip ratio  $R_s$ , depth  $h$ , effective diffusivity  $\eta$ .

plotted in Fig. 21.

Like in Case 1, at the sub-regime limits (corresponding to the large and stiff variations of  $\eta$ ), the relative error is higher (approximately 20% in  $h$ ) than anywhere else. Out of these stiff regime transition areas, the error on the depth  $h$  is small, lower than 7%; even lower in the sub-regime 1 area. Again the three estimates give accurate results in their respective domain of validity.

In comparison with the first guess, Fig. 19, the VDA process improves a bit the depth estimates in the inner parts of sub-regimes 2 and 3 and at the “sub-regimes boundaries” (making decrease the peak errors).

Concerning the friction coefficient  $C$  (which is computed a-posteriori), its accuracy is similar to the case of downstream measurements, see Fig.12. For this field  $C$ , the VDA process improves greatly its accuracy, in particular in the sub-regime 2 area. Typically the VDA process makes decrease the errors from 30% to less than 20% in the smooth areas; and from approximately 200% to 100% in the stiff transition areas.

### 6.3 On the robustness of the inversion method

As already noticed for the first guess, the present depth inference is (slightly) more accurate than in the downstream measurements case (Test case 1), compare Fig. 11 with Fig. 21. This result is only due to the better a-priori slip ratio law  $R_s^{(0)}$ , see the fitting law in Fig. 5 (Right). Also, Test case 2 results demonstrate the following important feature. Since the present depth inversions are based on an elliptic equation (and not a hyperbolic equation), the xSIA equation (14), then the depth measurements location is not important. Typically, measuring the depth at upstream, downstream or laterally, does not affect the inversion method accuracy. The important starting points of the present approach are the accuracy of the surface observations (the observational term  $Q_H$ ) and the accuracy of  $R_s^{(0)}$  derived from the depth measurements.

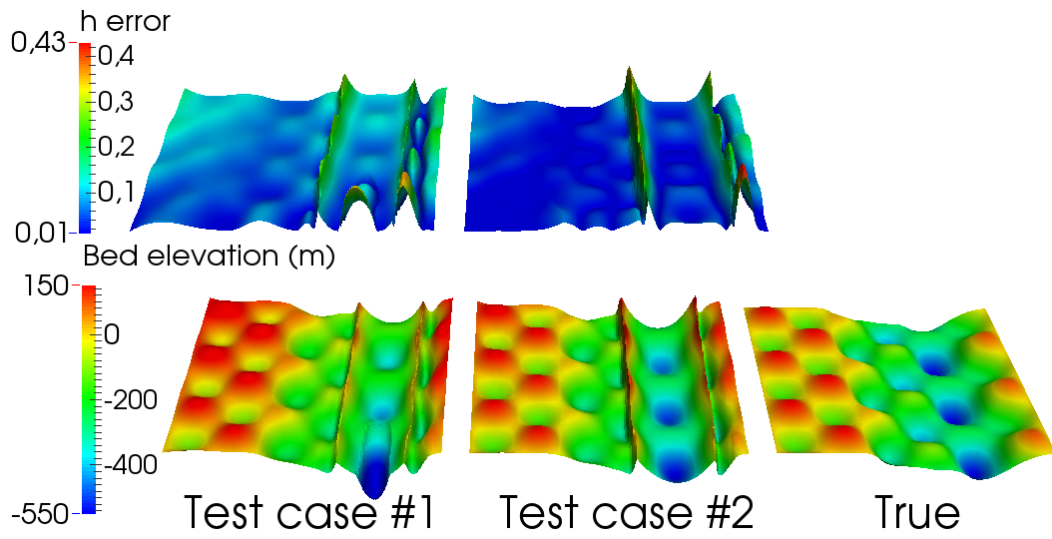


Figure 20: Bed elevation first guess  $b^{(0)}$ . (Down) from left to right: Test case 1, test case 2, true value. (Top) Corresponding relative errors.

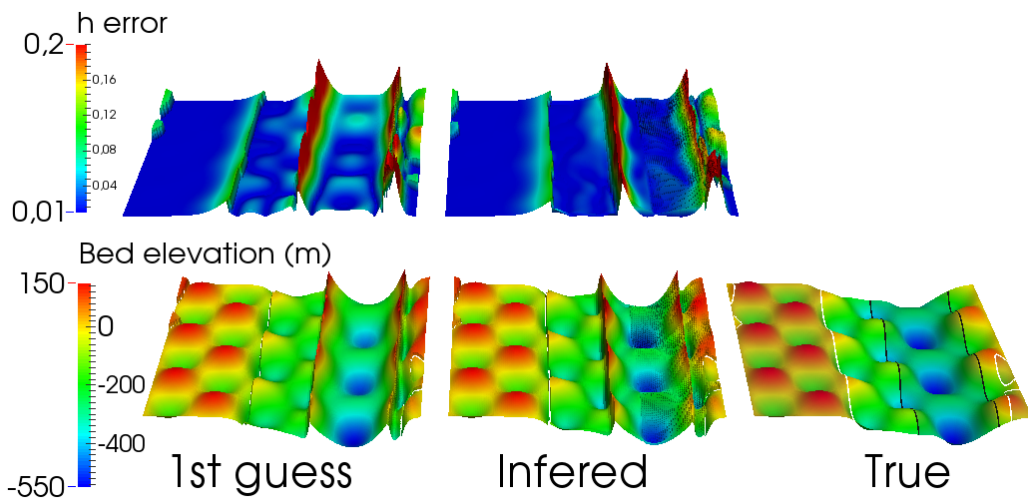


Figure 21: Test case 2: bed elevation after VDA. (Down) From left to right: first guess, inferred value after VDA, true value. (Top) Corresponding relative errors. The white lines denotes the sub-regime area boundaries defined from Table 1..

## 7 Inference of the correct slope scale in the xSIA model

As already discussed, a major difficulty to set up a SIA model is to manage its high sensitivity to the slope values  $\mathcal{S}$ . This sensitivity means sensitivity with respect to the slope error measurements but also with respect to the *slope scale definition* of the flow model. The latter is a global concept in space. Typically for the ice-sheets, out of ice-streams and/or far inland to be sub-regime 1 compatible, a standard accepted slope scale is approximately  $10h^*$ ,  $h^*$  being a characteristic thickness. Nevertheless, for more sliding flows (i.e. in sub-regime 2 and sub-regime 3 areas), this characteristic scale may have to be adapted, see e.g. [11, 26] for detailed analysis. From the present new depth estimations, let us propose two approaches to define the correct slope scale of a xSIA model (14).

A first approach would consist to infer correlations between the slope scale and the depth from the depth measurements (e.g. measurements based on the blue or red lines in Fig. 3 or based on the massive data sets available for the two ice-sheets[6], [2]). Indeed, from a data set providing all the model outputs (surface elevation, surface velocity and depth in particular), it is possible to infer an “optimal” slope scale. Then, given the numerical model (including the computational and bed topography grids), this optimal slope scale can be considered throughout the computational domain.

A complimentary second approach would rely on the few present depth estimations. First let us recall that the sub-regime 2 estimation, see (22) and (23), is valid everywhere i.e. it is valid in the three sub-regime areas (despite in practice it may be not necessarily the most accurate in sub-regime 1 area since numerical errors in  $R_s$  or  $\eta$ , see the discussion above and Fig. 10). Then the correct SIA model slope scale can be defined from the radically different behaviors of the depth estimations with respect to  $Q_H$ .

Indeed, the sub-regime 1 depth estimation (19) behaves in  $Q_H^{1/(q+1)}$  while the sub-regime 2 estimation (23) behaves in  $Q_H^{-1}$ . Therefore, given all the points located in the sub-regime 1 and sub-regime 2 areas (point set identified from a-priori values like Tab. 1 or from the a-priori slip ratio value  $R_s^{(0)}$ ), the two depth estimations can be computed from the observed slope value *at different slope scales* (e.g. at 1-5-10 mesh size or at 1-5-10 characteristic depth).

Then the correct slope scale (which is an uniform concept in the whole computational domain) is those giving the closest depth obtained from the *two* estimations. In other words, the correct scale corresponds to the *intersection point* between the  $h_{sr1}$  and  $h_{sr2}$  curves in Fig. 14. In a large set of data, the intersection point can be statistically estimated.

Since the present depth estimations are local, this method to infer the optimal / correct slope scale of the xSIA model can be illustrated for 1D uniform flows.

### 1D uniform flows, corresponding to the three sub-regimes.

Let us consider 1D uniform flows. The fluid properties ( $A, q, \rho$ ) are identical as previously and three typical flows are considered. For all three, the slope value is:  $\mathcal{S} = 0.2\%$ .

Each flow differs from each other by the values of  $\mathbf{u}_H$  and  $h$ . Then are evaluated: the observational term  $Q_H$ , the friction coefficient  $C$  from (26), the effective diffusivity  $\eta$  and the slip ratio  $R_s$ .

Finally, the three estimations (19), (23) and (25) can be computed. The three typical flows considered are the following.

- *Flow sr1* (highly sheared):  $\mathbf{u}_H = 5$  m/y and  $h = 2.10^3$ m.

It follows:  $Q_H \approx 19.8$ ,  $C \approx 2.20 \cdot 10^{-22}$ ,  $\eta \approx 4.19 \cdot 10^{-8}$  and  $R_s \approx 0.93$ .

The resulting three depth estimations are:  $h_{sr1} \approx 2035.7$ ,  $h_{sr2} \approx 2000.0$ ,  $h_{sr3} \approx 1627.3$ , see Fig. 22 for  $\mathcal{S} = 0.2\%$ .

Recall the true value is  $h = 2000$ ; as expected the  $h_{sr2}$  estimation is perfect since including all terms and evaluated from exact data.

The  $h_{sr1}$  estimation is 1.7% accurate because of the slip ratio value close to 1 (but with 7% slipping). Let us notice that with these data but  $C = 0$ , the surface velocity would be  $\mathbf{u}_H \approx 4.66$ m/y.

- *Flow sr2* (mildly sheared flow):  $\mathbf{u}_H = 20$  m/y and  $h = 2.10^3$ m.

It follows:  $Q_H \approx 79.3$ ,  $C \approx 9.88 \cdot 10^{-21}$ ,  $\eta \approx 1.96 \cdot 10^{-7}$  and  $R_s \approx 0.23$ .

The resulting three depth estimations are:  $h_{sr1} \approx 2878.9$ ,  $h_{sr2} \approx 2000.0$ ,  $h_{sr3} \approx 1906.8$ , see Fig. 22 for  $\mathcal{S} = 0.2\%$ .

Recall the true value is  $h = 2000$ . Again, as expected the  $h_{sr2}$  estimation is perfect.

The  $h_{sr1}$  estimation is incorrect (43.9% error); the  $h_{sr3}$  estimation is 4.7% accurate because of the slip ratio  $R_s$  value (which is quite low).

- *Flow sr3* (very weakly sheared flow):  $\mathbf{u}_H = 50$  m/y and  $h = 10^3$  m.

It follows:  $Q_H \approx 198.1$ ,  $C \approx 2.56 \cdot 10^{-19}$ ,  $\eta \approx 2.57 \cdot 10^{-7}$  and  $R_s \approx 5.8 \cdot 10^{-3}$ .

Let us notice that with these data but  $C = 0$ , it would give  $\mathbf{u}_H \approx 0.29$ m/y only.

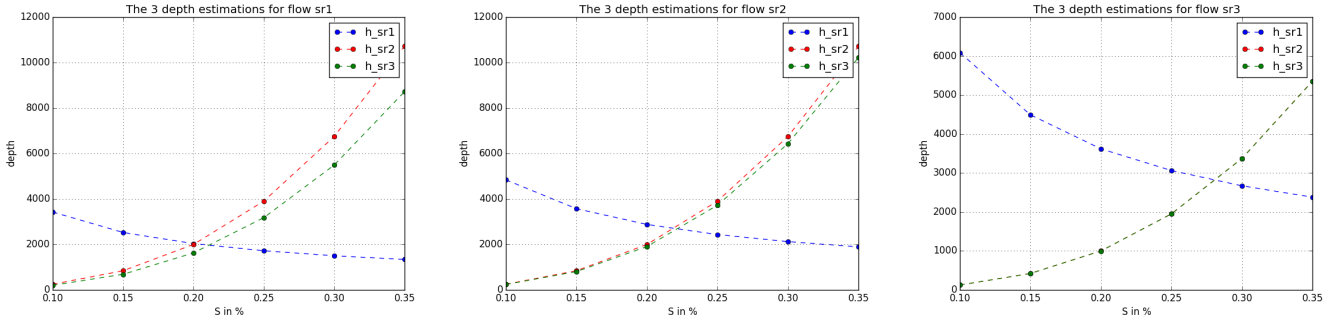


Figure 22: 1D uniform flows: the three depth estimations  $h_{sr\Box}$ . From left to right: sub-regime 1 case, sub-regime 2 case, sub-regime 3 case.

The resulting three depth estimations are:  $h_{sr1} \approx 3620.1$ ,  $h_{sr2} \approx 1000.0$ ,  $h_{sr3} \approx 998.8$ , see Fig. 22 for  $\mathcal{S} = 0.2\%$ .

Recall the true value is  $h = 2000$  (with the perfect  $h_{sr2}$  estimation again).

920 The  $h_{sr3}$  estimation is extremely accurate (0.12% error) since the slip ratio is extremely low. On the contrary, the  $h_{sr1}$  estimation is really wrong (262% error). As expected, the  $h_{sr1}$  estimation over estimates the true value.

These three typical examples highlight each depth estimation behavior and accuracy, depending on their respective domain of validity.

925 Next, the same computations are performed but by making vary the slope  $\mathcal{S}$  from  $\mathcal{S} = 0.1\%$  to  $0.35\%$  (recall that the reference - “true” value is  $\mathcal{S} = 0.2\%$ ). Making vary  $\mathcal{S}$  makes vary  $Q_H$ . The resulting curves are plotted in Fig. 22. In Fig. 22 (Right), the graphs of  $h_{sr2}$  and  $h_{sr3}$  are fully superposed. This curves illustrate the radically different behaviors of the explicit depth estimations with respect to  $\mathcal{S}$ .

It can be noticed that in sub-regime 1 case, the correct-sough slope value ( $\mathcal{S} = 0.2$ ) can be recovered by 930 detecting the intersection point between the two estimations  $h_{sr1}$  and  $h_{sr2}$ , see Fig. 22 (Left).

Since the sub-regime 1 estimation (19) over estimates the true value as soon as the sliding is not vanishing, then in the sub-regime 2 and sub-regime 3 areas, the intersection points give an upper-bound only of the correct depth, hence an upper-bound only of the correct slope value, see Fig. 22 (Middle) and (Right).

In other words, the present three depth estimations make possible to infer the correct slope scale to set up 935 consistently the xSIA models, if some depth measurements are available. Indeed, the approach detailed here in 1D can be applied in the 2D case since the estimations are point-wise. Then the inference of the correct slope scale from available complete data (including depth measurements) *in the weakly sheared areas (sub-regime 1 areas)* becomes possible. Next this optimal slope scale can be applied in the xSIA model throughout the computational domain (i.e. where depth data are not available and in the other sub-regime areas).

940

## 8 Conclusion & perspectives

945 This study proposes a new inverse method to infer the bottom topography  $b$  and the friction coefficient  $C$  in the Shallow Ice Approximation models. Then the method can be applied to the great majority of the ice sheet surfaces (sheared flow areas) and to many high mountain glaciers. In a mathematical point of view, the present inverse method can be applied to any shallow sheared generalized Newtonian fluid flow, for example lava flows (with the thermal field given), mud flows and many polymer flows. The method is based on the 950 definition of sub-regimes depending on the slip ratio, different combinations of explicit field expressions with a linear-quadratic optimal control problem solved by Variational Data Assimilation (where the direct equation is a gentle linear elliptic equation). This leads to a particularly robust method even in presence of uncertain surface measurements and independently of the depth measurement locations (on the contrary if inverting a regularized first order transport equation); also the potential various error measurements are damped (and 955 not propagated). Finally the difficult question aiming at determining the correct slope scale in a SIA model may be solved by cross-comparing the few depth estimations proposed. While assessing the method with few difficult academic multi-regime test cases, the method weakness turned out to be its relatively low accuracy in the stiff variation areas of the friction coefficient  $C$  (typically in canyon margins where  $C$  varies of few orders of

magnitude); however this demonstrates the method capability to infer a reliable bottom topography elevation  $b$  despite an extremely varying friction coefficient  $C$ . This new inverse method can be straightforwardly extended to unsteady flows if the available surface observations are time-dependent too. It will be assessed with real data sets in a forthcoming study

**Acknowledgements** The first author is deeply grateful to E. Larour, M. Morlighem, E. Rignot and H. Seroussi from JPL/Caltech-NASA and Univ. California of Irvine for co-funding him in 2014. The discussions the author had in this group greatly contributed to his understanding of data in glaciology and ice-flows in Antarctica.

The second author has been funded by CNES TOSCA grant (forthcoming NASA-CNES SWOT mission) during his INSA Master's degree internship, making possible the 2D Python/FEniCS computational code development used in this article.

## References

- [1] Martin Alnæs, Jan Blechta, Johan Hake, August Johansson, Benjamin Kehlet, Anders Logg, Chris Richardson, Johannes Ring, Marie E Rognes, and Garth N Wells. The fenics project version 1.5. *Archive of Numerical Software*, 3(100):9–23, 2015.
- [2] JL Bamber, JA Griggs, RTWL Hurkmans, JA Dowdeswell, SP Gogineni, I Howat, J Mouginot, J Paden, S Palmer, E Rignot, et al. A new bed elevation dataset for greenland. *The Cryosphere*, 7(2):499–510, 2013.
- [3] M Boutounet, J Monnier, and J-P Vila. Multi-regime shallow free surface laminar flow models for quasi-newtonian fluids. *European Journal of Mechanics-B/Fluids*, 55:182–206, 2016.
- [4] Anne-Laure Dalibard and David Gérard-Varet. Effective boundary condition at a rough surface starting from a slip condition. *Journal of Differential Equations*, 251(12):3450–3487, 2011.
- [5] A. C. Fowler. *Mathematical geoscience*, volume 36. Springer, 2011.
- [6] P Fretwell, Hamish D Pritchard, David G Vaughan, JL Bamber, NE Barrand, R Bell, C Bianchi, RG Bingham, DD Blankenship, G Casassa, et al. Bedmap2: improved ice bed, surface and thickness datasets for antarctica. *The Cryosphere*, 7(1), 2013.
- [7] Pierre-André Garambois and Jérôme Monnier. Inference of effective river properties from remotely sensed observations of water surface. *Advances in Water Resources*, 79:103–120, 2015.
- [8] David Gilbarg and Neil S Trudinger. *Elliptic partial differential equations of second order*. springer, 2015.
- [9] Ronald Glowinski and Patrick Le Tallec. *Augmented Lagrangian and operator-splitting methods in nonlinear mechanics*, volume 9. SIAM, 1989.
- [10] R. Greve and H. Blater. *Dynamics of Ice Sheets and Glaciers*. Advances in Geophysical and Environmental Mechanics and Mathematics. 2009.
- [11] G Hilmar Gudmundsson. Transmission of basal variability to a glacier surface. *Journal of Geophysical Research: Solid Earth*, 108(B5), 2003.
- [12] G Hilmar Gudmundsson and Melanie Raymond. On the limit to resolution and information on basal properties obtainable from surface data on ice streams. *The Cryosphere Discussions*, 2(3):413–445, 2008.
- [13] GH Gudmundsson. Analytical solutions for the surface response to small amplitude perturbations in boundary data in the shallow-ice-stream approximation. *The Cryosphere*, 2(2):77–93, 2008.
- [14] Per Christian Hansen and Dianne Prost O’Leary. The use of the l-curve in the regularization of discrete ill-posed problems. *SIAM Journal on Scientific Computing*, 14(6):1487–1503, 1993.
- [15] C Heining and M Sellier. Direct reconstruction of three-dimensional glacier bedrock and surface elevation from free surface velocity.
- [16] Marc Honnorat, Jérôme Monnier, Nicolas Rivière, Étienne Huot, and François-Xavier Le Dimet. Identification of equivalent topography in an open channel flow using lagrangian data assimilation. *Computing and visualization in science*, 13(3):111–119, 2010.

- 1005 [17] Matthias Huss and Daniel Farinotti. A high-resolution bedrock map for the antarctic peninsula. *The Cryosphere*, 8(4):1261–1273, 2014.
- [18] K. Hutter. *Theoretical Glaciology*. 1983.
- [19] Guillaume Jouvet and Ed Bueler. Steady, shallow ice sheets as obstacle problems: well-posedness and finite element approximation. *SIAM Journal on Applied Mathematics*, 72(4):1292–1314, 2012.
- 1010 [20] Guillaume Jouvet, Jacques Rappaz, Ed Bueler, and Heinz Blatter. Existence and stability of steady-state solutions of the shallow-ice-sheet equation by an energy-minimization approach. *Journal of Glaciology*, 57(202):345–354, 2011.
- [21] E Larour, J Utke, B Csatho, A Schenk, H Seroussi, M Morlighem, E Rignot, N Schlegel, and A Khazendar. Inferred basal friction and surface mass balance of the northeast greenland ice stream using data assimilation of icesat (ice cloud and land elevation satellite) surface altimetry and issm (ice sheet system model). *Cryosphere*, 8(6), 2014.
- 1015 [22] François-Xavier LeDimet and Olivier Talagrand. Variational algorithms for analysis and assimilation of meteorological observations: theoretical aspects. *Tellus A*, 38(2):97–110, 1986.
- [23] Anders Logg, Garth N Wells, and Johan Hake. Dolfin: A c++/python finite element library. In *Automated Solution of Differential Equations by the Finite Element Method*, pages 173–225. Springer, 2012.
- 1020 [24] Nathan Martin and Jérôme Monnier. Adjoint accuracy for the full-stokes ice flow model: limits to the transmission of basal friction variability to the surface. *The Cryosphere*, 8:721–741, 2014.
- [25] Nathan Martin and Jérôme Monnier. Four-field finite element solver and sensitivities for quasi-newtonian flows. *SIAM Journal on Scientific Computing*, 36(5):S132–S165, 2014.
- 1025 [26] Nathan Martin and Jérôme Monnier. Inverse rheometry and basal properties inference for pseudoplastic geophysical flows. *European Journal of Mechanics-B/Fluids*, 50:110–126, 2015.
- [27] Laurent Michel, Marco Picasso, Daniel Farinotti, Andreas Bauder, Martin Funk, and Heinz Blatter. Estimating the ice thickness of mountain glaciers with an inverse approach using surface topography and mass-balance. *Inverse Problems*, 29(3):035002, 2013.
- 1030 [28] Laurent Michel, Marco Picasso, Daniel Farinotti, Martin Funk, and Heinz Blatter. Estimating the ice thickness of shallow glaciers from surface topography and mass-balance data with a shape optimization algorithm. *Computers & Geosciences*, 66:182–199, 2014.
- [29] J. Monnier. *Variational data assimilation: from optimal control to large scale data assimilation*. Open Online Course (videos) with the accompanying manuscript (143 pages). INSA - University of Toulouse, 2014.
- 1035 [30] J. Monnier, P. Brisset, C. Couderc, and P.A. Garambois. *DassFlow: Data Assimilation for Free Surface Flows*. <http://www.math.univ-toulouse.fr/DassFlow>. CNES, CNRS, INSA group, university of Toulouse.
- [31] L. W. Morland. Thermo-mechanical balances of ice sheet flow. *Geophysical and Astrophysical Fluid Dynamics*, 29:237–266, 1984.
- 1040 [32] M Morlighem, E Rignot, J Mouginot, H Seroussi, and E Larour. Deeply incised submarine glacial valleys beneath the greenland ice sheet. *Nature Geoscience*, 7(6), 2014.
- [33] M Morlighem, E Rignot, J Mouginot, H Seroussi, and E Larour. High-resolution ice-thickness mapping in south greenland. *Annals of Glaciology*, 55(67):64–70, 2014.
- 1045 [34] Mathieu Morlighem. *Ice sheet properties inferred by combining numerical modeling and remote sensing data*. PhD thesis, Ecole Centrale Paris, 2011.
- [35] Mathieu Morlighem, E Rignot, Hélène Seroussi, Eric Larour, H Ben Dhia, and Denis Aubry. A mass conservation approach for mapping glacier ice thickness. *Geophysical Research Letters*, 38(19), 2011.
- [36] LA Rasmussen. Bed topography and mass-balance distribution of columbia glacier, alaska, usa, determined from sequential aerial photography. *Journal of Glaciology*, 34(117):208–216, 1988.
- 1050 [37] E Rignot, J Mouginot, and B Scheuchl. Ice flow of the antarctic ice sheet. *Science*, 333(6048):1427–1430, 2011.

- [38] C. Schoof and C.A. Hindmarsh. Thin-film flows with wall slip: an asymptotic analysis of higher order glacier flow models. *Q. Jl Mech. Appl. Math.*, 63(1):73–114, 2010.
- [39] Mathieu Sellier. Inverse problems in free surface flows: a review. *Acta Mechanica*, 227(3):913–935, 2016.
- 1055 [40] Mathieu Sellier, A Gessese, and C Heining. Analytical and numerical bedrock reconstruction in glacier flows from free surface elevation data. 2012.
- [41] Throstur Thorsteinsson, Charles F Raymond, G Hilmar Gudmundsson, Robert A Bindschadler, Paul Vornberger, and Ian Joughin. Bed topography and lubrication inferred from surface measurements on fast-flowing ice streams. *Journal of Glaciology*, 49(167):481–490, 2003.
- 1060 [42] Roland C Warner and WF Budd. Derivation of ice thickness and bedrock topography in data-gap regions over antarctica. *Annals of Glaciology*, 31(1):191–197, 2000.